

DISSERTATION

ELECTROLUMINESCENCE OF THIN-FILM CdTe SOLAR CELLS AND MODULES

Submitted by

John Michael Raguse

Department of Physics

In partial fulfillment of the requirements

For the Degree of Doctor of Philosophy

Colorado State University

Fort Collins, Colorado

Summer 2015

Doctoral Committee:

Advisor: James Sites

Martin Gelfand

Marko Topič

W. S. Sampath

Jose de la Venta

Copyright by John Raguse 2015

All Rights Reserved

ABSTRACT

ELECTROLUMINESCENCE OF THIN-FILM CdTe SOLAR CELLS AND MODULES

Thin-film photovoltaics has the potential to be a major source of world electricity. Mitigation of non-uniformities in thin-film solar cells and modules may help improve photovoltaic conversion efficiencies. In this manuscript, a measurement technique is discussed in detail which has the capability of detecting such non-uniformities in a form useful for analysis.

Thin-film solar cells emit radiation while operating at forward electrical bias, analogous to an LED, a phenomena known as electroluminescence (EL). This process relatively is inefficient for polycrystalline CdTe devices, on the order of $10^{-4}\%$, as most of the energy is converted into heat, but still strong enough for many valuable measurements. A EL system was built at the Colorado State University Photovoltaics Laboratory to measure EL from CdTe cells and modules.

EL intensity normalized to exposure time and injection current density has been found to correlate very well with the difference between ideal and measured open-circuit voltage from devices that include a GaAs cell, an AlGaAs LED, and several CdTe cells with variations in manufacturing. Furthermore, these data points were found to be in good agreement when overlaid with calibrated data from two additional sources. The magnitude of the inverse slope of the fit is in agreement with the thermal voltage and the intercept was found to have a value near unity, in agreement with theory. The expanded data set consists of devices made from one of seven different band gaps and spans eight decades of EQE_{LED} efficiencies. As expected, cells which exhibit major failure of light-dark J-V superposition did not follow trend of well-behaved cells.

EL images of selected defects from CdTe cells and modules are discussed and images are shown to be highly sensitive to defects in devices, since the intensity depends exponentially on the cells' voltages. The EL technique has proven to be a useful high-throughput tool for screening of cells. In addition to EL images, other opto-electronics characterization

techniques were used to analyze defects in cells and modules such as weak-diode areas, cell delineation near substrate edge, non-uniform chlorine passivation, holes in back contact, high-resistance foreign layer, high back-contact sheet resistance, a discontinuous P3 line scribe (intercell shunt) and shunt through a cell (intracell shunt).

Although EL images are proficient at illustrating the location and severity of defects with potentially high spatial resolution and short measurement times, their ability to identify the cause of such defects is limited. EL in concert with Light-Beam-Induced Current (LBIC), however, makes for a powerful ensemble as LBIC can probe different film layers at arbitrary voltage bias conditions, albeit with increased measurement times and potentially reduced spatial resolution.

ACKNOWLEDGMENTS

I would like to extend my sincere gratitude to my adviser, Jim Sites. Thank you for believing in me, helping me continually hone my skills and providing me with the resources to grow and develop as a scientist.

Thank you also to W.S. Sampath for demonstrating the importance of setting goals and the sacrifices sometimes required to achieve those goals. Thank you to Marko Topič, your help with EL since its beginning at CSU has helped frame the problem and was critical in getting much of the work presented here sorted out.

Thank you to all of the members of my family who have been so patient and encouraging of my decisions. Most notably, I would like to thank my mother, Margaret, who has sacrificed for me. I am appreciative of you and what you have done for me, I would not of achieved this goal if it were not for your love and support. Thank you also to Dan who first introduced me to the world of physics so long ago. I would like to thank my father, John, who has instilled a strong work ethic in me since I was young.

I would like to thank my friends and colleagues in both Jim's and Sampath's laboratory: Russell Geisthardt, Pavel Kobayakov, Jason Kephardt, Drew Swanson, Kevan Cameron, Andrew Moore, Amit Munshi, Katherine Zaunbrechner, Tao Song, Valerie Jacobson and Tyler McGoffin. Our conversations were more fruitful than any PV book. I have very much enjoyed the years we have spent working together. Lastly, I would like to thank my dear friend, Sam Ronald, for the countless conversations we have had together and helping me see the other side of the coin.

I would like to thank Anders Olsen and Alan Davies of Abound Solar for providing me with samples as well as for the fruitful conversations which we had together. Thank you also to Markus Gloeckler of First Solar for sending me some state-of-the-art CdTe cells.

I would like to thank Robert Adame of the physics machine shop. Your guidance has significantly improved every tool which I have worked on (inside and outside the lab).

Lastly, I would like to thank the funding agencies who supported this work, the Department of Energy's F-PACE and the National Science Foundation I/UCRC.

TABLE OF CONTENTS

Abstract	ii
Acknowledgments	iv
Table of Contents	vi
List of Tables	viii
List of Figures	ix
1 Introduction	1
1.1 Motivation	1
1.2 Cadmium Telluride Solar Cells	1
1.3 Manufacturing of CdTe Solar Cells at CSU	2
1.4 Electrical Characterization Measurements of Solar Cells	4
1.4.1 Current Density vs Voltage Curves	4
1.4.2 Electroluminescence	6
1.4.3 Quantum Efficiency	7
1.4.4 Estimating Band Gap From Quantum Efficiency	8
1.4.5 Light-Beam-Induced Current	10
2 Electroluminescence System	12
2.1 Overview of Experimental Setup	12
2.2 Detector Array	14
2.3 Shutter Speed	17
2.4 Optics	18
2.5 Image Correction	19
2.6 Background Levels	20
2.7 Calibration	22
2.7.1 Absolute Calibration of Pixel Size	22
2.7.2 Calibration of Pixel Response	23
2.8 Experimental Details	26
2.9 Image Processing	27
2.9.1 Look-Up Table	29
2.10 Calculating Area From Electroluminescence Image	29
3 EL Intensity and its Relationship to Cell Voltage	32
3.1 Open-Circuit Voltage Correction Offset	33
3.2 Derivation of External Quantum Efficiency of an LED	34
3.3 Results	36
3.4 EL Uniformity	39
3.5 Breakdown of the Reciprocity Relationship	41
3.6 Temperature Dependent EL	42
3.7 Summary of EL Intensity-Voltage Deficit Relationship	44

4	Inhomogeneities in Small-Area Cells	45
4.1	Typical CSU CdTe Cell	47
4.2	Weak-Diode Areas	49
4.3	Cell Delineation in Delete Region	52
4.4	Non-Uniform Chlorine Passivation	54
4.5	Holes in Back Contact	55
4.6	Back-Contact Sheet Resistance	58
4.7	High-Resistance Foreign Layer	60
4.8	Summary of Inhomogeneities in Small-Area Cells	61
5	Defects in Modules.	63
5.1	Discontinuous P3 Line Scribe	67
5.2	Shunt Through Cell	69
5.3	Summary of Defects in Modules	71
6	Conclusions and Future Work	72
6.1	Conclusions	72
6.2	Recommendations for Future Work	73
	Bibliography.	75

LIST OF TABLES

1.1	Calculated J-V parameters from the typical CSU CdTe cell	6
2.1	Specifications for CCD detector array.	16
2.2	Typical programmed values for detector	27
3.1	Voltage deficit and EQE_{LED} values for various cells	37
3.2	EQE_{LED} -voltage deficit-temperature fit parameters	44
4.1	Defects identified in cells	46
5.1	Defects identified in modules.	66

LIST OF FIGURES

1.1	Schematic of typical CSU CdTe cell.	2
1.2	Various steps during typical CSU CdTe solar cell deposition process	3
1.3	J-V curve from typical CSU CdTe cell and equivalent electrical circuit.	4
1.4	Schematic of EL emission.	6
1.5	QE curve from typical CSU CdTe cell	8
1.6	Differential QE and EL spectra	9
1.7	Cell bias conditions during LBIC measurement	11
2.1	Schematic of EL system.	13
2.2	Detector array response curve	15
2.3	Saturation of detector array	15
2.4	Accuracy of programmed exposure time	17
2.5	Transmission of optical filter used in EL system.	19
2.6	Artifact from imaging optics	20
2.7	Mean background pixel response.	21
2.8	Verification of absolute calibration of pixel size	23
2.9	Typical EL spectrum from calibration LED	23
2.10	EL image of calibration LED.	24
2.11	Calibration of pixel response	25
2.12	Image processing steps	28
2.13	NIRR image of cell with standard and inverted LUT	29
2.14	Calculating luminescent area of cell from EL image.	31
2.15	Line scribe across cell	31
3.1	Normalized EL intensity vs decreasing V_{OC}	34
3.2	Normalized EL Intensity vs voltage deficit	38

3.3	EQE_{LED} vs voltage deficit	39
3.4	Cells of non-uniform EL intensity	40
3.5	Histogram of EL images	41
3.6	Breakdown of reciprocity relationship.	42
3.7	EL vs voltage deficit at different cell temperatures	43
4.1	EL image, NIR image, LBIC maps and J-V curve of typical CSU CdTe cell.	48
4.2	Cell with weak-diode areas	50
4.3	EL images and histograms of cells with weak-diode areas	52
4.4	Cell delineated in delete region	53
4.5	Cells with non-uniform chlorine passivation treatment	55
4.6	Schematic of CdTe cell with holes in back contact	56
4.7	Cell with holes in back contact	57
4.8	Cell with high back-contact sheet resistance	59
4.9	Cell with high-resistance foreign layer.	60
5.1	Schematic of cross-section of well-behaved module	63
5.2	EL image of well-behaved module	65
5.3	EL image of module with defects	66
5.4	EL image of module with discontinuous P3 line scribe	67
5.5	Schematic of module with discontinuous P3 line scribe.	68
5.6	Line cut of module with discontinuous P3 line scribe	68
5.7	EL image of module with shunt through cell.	69
5.8	Line cut of module with shunt through cell	70
5.9	Schematic of module with shunt through cell	71

Chapter 1

INTRODUCTION

1.1 Motivation

Current human activity is not sustainable as atmospheric carbon dioxide (CO_2) levels have recently approached a level not seen in recorded history of 400 ppm [1]. The 2014 Intergovernmental Panel on Climate Change (IPCC) report claims with a certainty of over 95% that global climate change is due to the anthropomorphic emission of green house gasses (GHG) emissions, such as CO_2 [2]. Furthermore, the report claims that as a result of GHG emissions, humans are causing irreversible damage to the Earth such as increase in the temperature of the ocean and atmosphere, diminishing levels of ice and snow and an increase in sea levels. Reduced emission of CO_2 will help mitigate these impacts. One of the key avenues in doing so is the implementation of low-carbon-emitting energy generation sources such as solar photovoltaics (PV).

1.2 Cadmium Telluride Solar Cells

There are several promising technologies for low-cost PV electricity. Of those technologies, Cadmium Telluride (CdTe) stands out as a proven technology partially due to its high absorption coefficient [3], near-optimum band gap [4] and low cost of manufacturing [5]. Like most solar cells, Cadmium Telluride (CdTe) solar cells consist of an n- and p-type semiconductor, however these devices are typically in a supersaturate configuration with an n-type Cadmium Sulfide (CdS) window layer and a p-type CdTe absorber layer. Although most of the devices presented in this manuscript were manufactured at CSU, some of the cells mentioned were manufactured by First Solar, a company which manufactures state-of-the-art CdTe solar cells and modules.

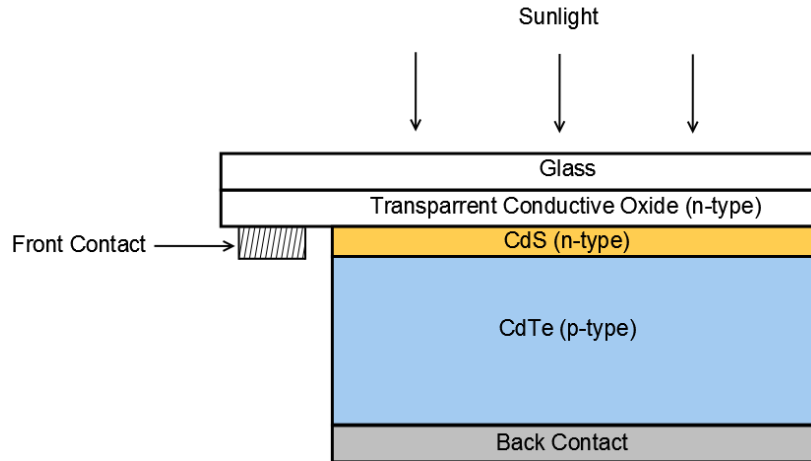


Figure 1.1: Schematic of a solar cell in superstrate configuration with a CdS window layer and a CdTe absorber layer.

Fig. 1.1 is a schematic of a CdTe cell in supersaturate configuration with the transparent conductive oxide (TCO) layer for electrical contacting, the CdS window layer, the CdTe absorber layer and electrical back-contact.

1.3 Manufacturing of CdTe Solar Cells at CSU

Many of the devices discussed in this manuscript were manufactured in Prof. W.S. Sampath's laboratory with a deposition system referred as the Advanced Research Deposition System (ARDS). The ARDS is a programmable tool employing a close-space sublimation (CSS) technique for the manufacturing of thin-film CdTe solar cells. The ARDS has an arm which is able to mechanically position the substrate over different sources, each of which can be loaded with a different material for sublimation. Film thickness is controlled by either length of time the substrate is exposed to a deposition source or temperature of deposition source. The ARDS is capable of processing 9 substrates a day; each substrate is delineated into 9 cells with a typical photovoltaic conversion efficiency of 12% under standard test conditions.

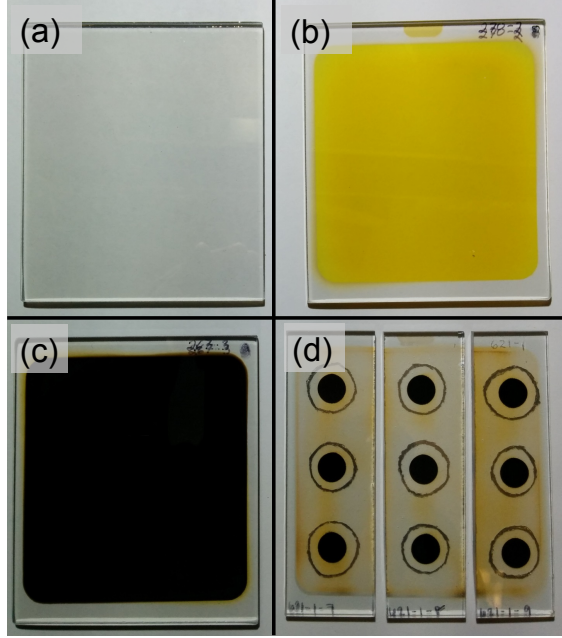


Figure 1.2: Various steps during the manufacturing process of CdTe solar cells: (a) TEC-10 glass, (b) TEC-10/CdS, (c) TEC-10/CdS/CdTe, (d) TEC-10/CdS/CdTe/back-contact/delineated cells (finished product).

The substrate used for deposition is commercially-available (Pilkington TEC-10) transparent-conductive-oxide (TCO) coated glass of dimensions $3.1 \times 3.6 \times 0.1250$ inches, see Fig. 1.2(a). After loading the clean substrate onto the ARDS and heating to appropriate temperature, ~ 120 nm of CdS and $\sim 2 \mu\text{m}$ of CdTe film are deposited sequentially, see Fig. 1.2(b) and (c) respectively. This process is followed by exposing the film stack to CdCl₂ vapor to passivate the polycrystalline CdTe material, a critical step in manufacturing of polycrystalline CdTe cells of respectable efficiency [6, 7, 8, 9]. The stack is then exposed to CuCl vapor for doping purposes. The substrate is next removed from the ARDS and rinsed with de-ionized water to remove any CdCl₂ salt build-up. The two-part back-contact is applied sequentially, a carbon/acrylic layer followed by a less-resistive nickel/acrylic layer. After drying of the painted back-contact, the stack is delineated into 9 circular cells of approximate diameter 1 cm and surrounded by a indium ring to contact the front TCO, see Fig. 1.2(d).

1.4 Electrical Characterization Measurements of Solar Cells

Following the completion of the solar-cell devices, their photovoltaic conversion efficiencies are measured. This may be followed by additional measurements to improve the understanding of the relationship between the cell manufacturing recipe and its resulting electrical behavior. This section discusses some of the measurement techniques used to understand such behavior.

1.4.1 Current Density vs Voltage Curves

The fundamental electrical characterization measurement of a solar cell is its measured current-density as a function of applied voltage bias (J-V) curve. This curve is typically measured under two illumination conditions: no illumination and standard illumination. Standard illumination is referred to as Air Mass 1.5 (AM 1.5) illumination, the standardized spectrum adopted by the community when measuring the efficiency of most solar cells [10]. Its intensity is standardized to 100 mW/cm^2 .

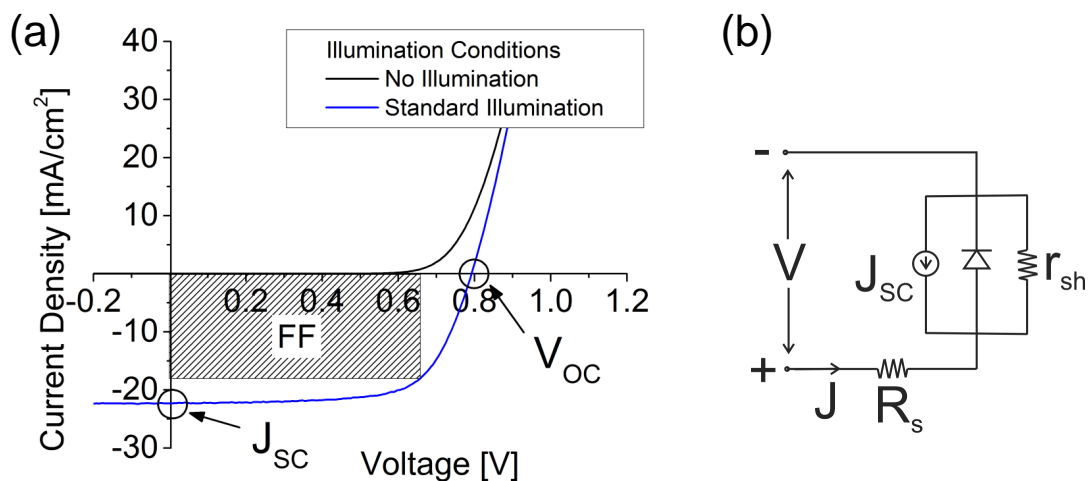


Figure 1.3: (a) J-V curve of a typical CSU CdTe cell and (b) equivalent circuit of a solar cell.

Fig. 1.3(a) is the J-V curve from the typical CSU CdTe cell, representative of the typical CdTe cell made with the ARDS deposition system. Three points of interest are highlighted

on the curve: short-circuit current density (J_{SC}), open-circuit voltage (V_{OC}) and fill-factor (FF), the ratio of maximum output power density to the product of J_{SC} with V_{OC} , i.e., the squareness of the light J-V curve . A cell's photovoltaic conversion efficiency is expressed as Eq. 1.1 below,

$$\eta = \frac{J_{SC}[\text{mA}/\text{cm}^2] \cdot V_{OC}[\text{V}] \cdot FF}{100 \text{ mW}/\text{cm}^2} \quad (1.1)$$

Where $J_{SC} \cdot V_{OC} \cdot FF$ is the maximum output power density of the cell and $100 \text{ mW}/\text{cm}^2$ is the approximate incident illumination power density under AM 1.5 illumination conditions. The characteristic diode equation of a solar cell describing the electrical behavior in Fig. 1.3(a) is given by Eq. 1.2 below,

$$J = J_0(e^{q(V-R_s J)/Ak_b T} - 1) - J_{SC} + \frac{V - JR_s}{r_{sh}}, \quad (1.2)$$

where J_0 is the saturation current density, R_s is the series resistance, r_{sh} is the shunt resistance, $\frac{k_b T}{q}$ is the thermal voltage and A is the diode quality factor ($1 \leq A \leq 2$). The equivalent circuit of a solar cell described by this equation is depicted in Fig. 1.3(b). For a well-behaved cell, the current through the shunt resistor is small ($J_{SC} \gg \frac{V-JR_s}{r_{sh}}$) and the voltage drop across the series resistance is small ($V \gg R_s J$). Employing these approximations simplifies Eq. 1.2 as Eq. 1.3 below,

$$J = J_0(e^{qV/Ak_b T} - 1) - J_{SC} \quad (1.3)$$

Well-behaved cells mentioned later in this manuscript will assume behavior approaching that described by Eq. 1.3. Calculated J-V parameters for the typical CSU CdTe cell from Fig. 1.3(a) are listed below in Table 1.1.

Table 1.1: Measured parameters from J-V curve presented in Fig. 1.3(a)

J_{SC} [mA/cm ²]	V_{OC} [V]	FF	η [%]	r_{sh} [$\Omega \cdot \text{cm}^2$]	J_0 [mA/cm ²]	R_s [$\Omega \cdot \text{cm}^2$]	A
22.3	0.797	0.69	12.3	7×10^2	3×10^{-6}	2.3	2

1.4.2 Electroluminescence

Electroluminescence (EL) is the spontaneous emission of radiation in a semiconductor as a result of electrical injection of free carriers, akin to the principle light emission of an LED and is the reciprocal process of a solar cell in its intended mode of operation [11]. Fig. 1.4 is a schematic depicting EL emission before and after the recombination process.

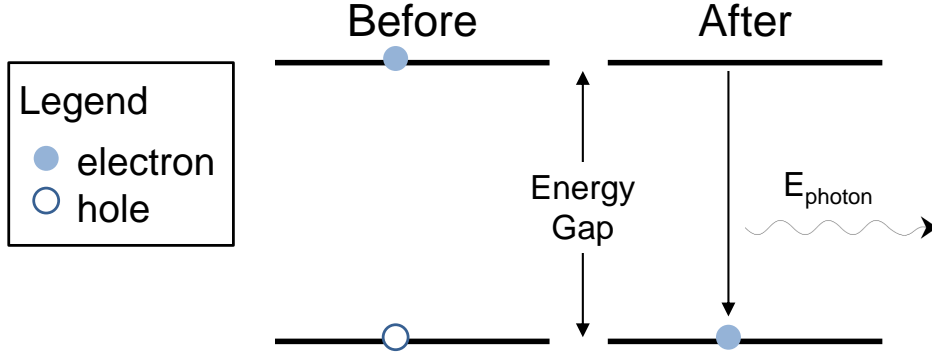


Figure 1.4: EL emission from a semiconductor - free electron injected into semiconductor radiatively recombines with a free hole; the photon emission energy near that of the band gap.

EL emission from CdTe solar cells operating in forward electrical bias is a near band-to-band transition in the CdTe film, where free electrons injected into the absorber material recombine with free holes. This process, however, is relatively inefficient for polycrystalline CdTe cells, $\sim 10^{-4}\%$ [12], since most of the recombination is non-radiative and results in the material increasing in temperature. Since the EL intensity is nearly proportional to the number of injected carriers, the experiments presented here were performed with the devices operating in constant-current mode. EL radiation may be analyzed either spectrally

or spatially, however the focus of the work presented here is on the spatial distribution of EL radiation from a photovoltaic device.

1.4.3 Quantum Efficiency

The quantum efficiency (QE) of a solar cell is the ratio of the number of collected electrons to the number of photons incident to the device as a function of photon energy. It is typically performed with the cell under no voltage bias and can be used as an independent verification of J_{SC} under AM 1.5 conditions.

$$QE(\lambda) = \frac{\text{no. of collected electrons}}{\text{no. of incident photons } (\lambda)} \quad (1.4)$$

Fig. 1.5 is a QE curve from the typical CSU CdTe solar cell; see Fig. 1.3(a) for cell's J-V curve. There are three regimes in the QE curve for this cell-type. The first is long-wavelength photons whose energies are less than the CdTe absorber band gap and contribute a relatively small amount to the photocurrent. The second regime is for photons whose energies are greater than the CdTe band gap but less than the CdS band gap. They are responsible for much of the photocurrent. The remaining region is for photons whose energies are greater than the CdS band gap in which only the fraction of light which has transmitted through the CdS film and absorbed by the CdTe film contributes to the photocurrent. This region is sensitive to CdS film thickness, since CdS is a direct band gap semiconductor [11].

A cell's short-circuit current density can be calculated by integrating a cell's QE response weighted by the AM 1.5 solar spectrum, expressed in photon-flux units, see Eq. 1.5.

$$J_{SC} = q \int_0^{\infty} QE(\lambda) AM1.5(\lambda) d\lambda \quad (1.5)$$

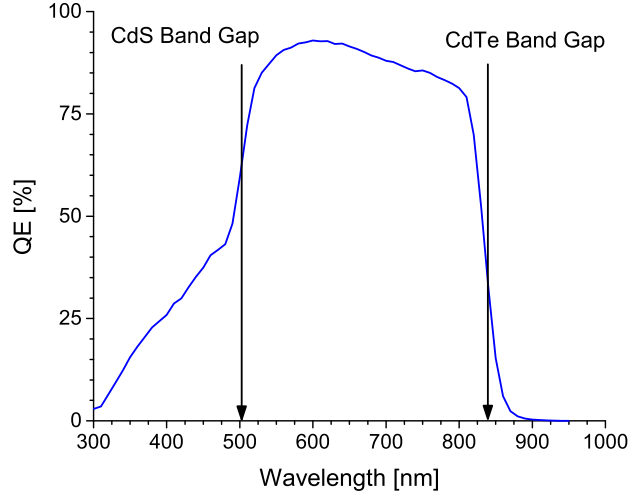


Figure 1.5: Typical QE curve from a solar cell with a cadmium sulfide window layer and a cadmium telluride absorber layer with their respective approximated band gaps labeled.

1.4.4 Estimating Band Gap From Quantum Efficiency

QE curves may be used to estimate the band gap of a cell and is a highly practical technique since unlike most other techniques used to estimate a cell's band gap, QE may be performed on a completed cell and is a standard measurement in most photovoltaic characterization labs.

The technique adopted in the CSU Photovoltaics Laboratory to estimate the band gap of the absorber film is the maximum absolute value of the derivative of QE curve with respect to photon wavelength. Fig. 1.6(a) is such a plot with the typical CSU CdTe cell and a First Solar cell. A peak centered very near the band gap can be observed with gaussian fits overlaid. The center of the gaussian fits are labeled with a precision of 0.005 eV. The peaks of the differential QE curves correspond to a absolute QE response of approximately 35% as labeled in Fig. 1.5 for CdTe.

EL spectra normalized to exposure time measured from CSU and First Solar CdTe cells is presented in Fig. 1.6(b). As depicted in Fig. 1.4 and discussed elsewhere [11, 13], spectral EL may be a useful technique in identifying the band gap of a cell. The energies of peaks are

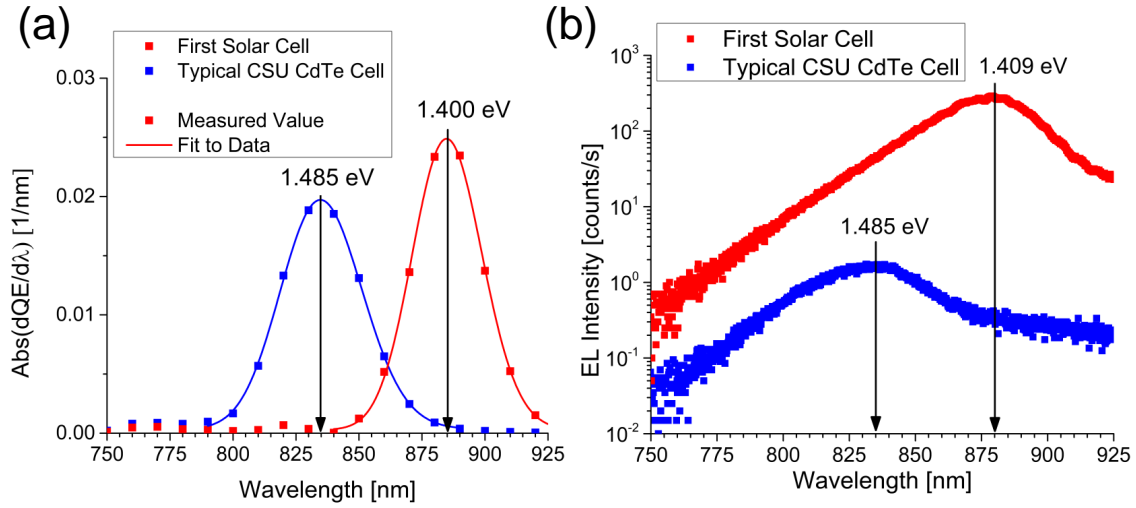


Figure 1.6: (a) Derivative of QE graph with respect to photon wavelength, used to estimate band gap of device, compiled by Dr. Russell Geisthardt and (b) measured EL spectra from the typical CSU CdTe cell and a cell manufactured by First Solar.

labeled, and they are near agreement with peak identified from differential QE measurement, thus giving an independent verification of method used.

The spectral EL data was collected with the assistance of Timothy Walton in Prof. William Fairbank’s research group at CSU.

1.4.5 Light-Beam-Induced Current

Unlike QE which measures the spectral response of a single position on a cell, light-beam-induced current (LBIC) maps the cell's response over all positions of a cell with a single illumination wavelength. Although the scanning area and resolution may vary, a measurement rate of approximately 17 data points/second is kept constant, thus, in practice, a scan area of 1×1 cm with a resolution of $100 \mu\text{m}/\text{pixel}$ and a measurement time of ~ 40 minutes is used. LBIC maps presented here were measured by Dr. Russell Geisthardt.

Fig. 1.7(a) is the QE curve of the typical CSU CdTe cell with two wavelengths used for LBIC scans highlighted. The shorter-wavelength 405-nm laser diode is typically used to measure variations in CdS film thickness, where as the longer-wavelength 638-nm laser diode is intended to probe the CdTe film near the main junction (absorption coefficient of approximately $5 \mu\text{m}^{-1}$ [3]). Fig. 1.7(b) is a J-V curve of typical CSU CdTe cell with the two voltage biases used highlighted. The larger-voltage bias may be used to probe local areas of the diode which prematurely turn-on, electrically equivalent to an increase in the saturation current density, J_0 , from Eq. 1.3. The LBIC system presented here is well-designed to identify a large variety of defects in cells albeit with long measurement times (~ 40 minutes/ 1 cm^2 scan area) and reduced spatial resolution ($\sim 100 \mu\text{m}/\text{pixel}$).

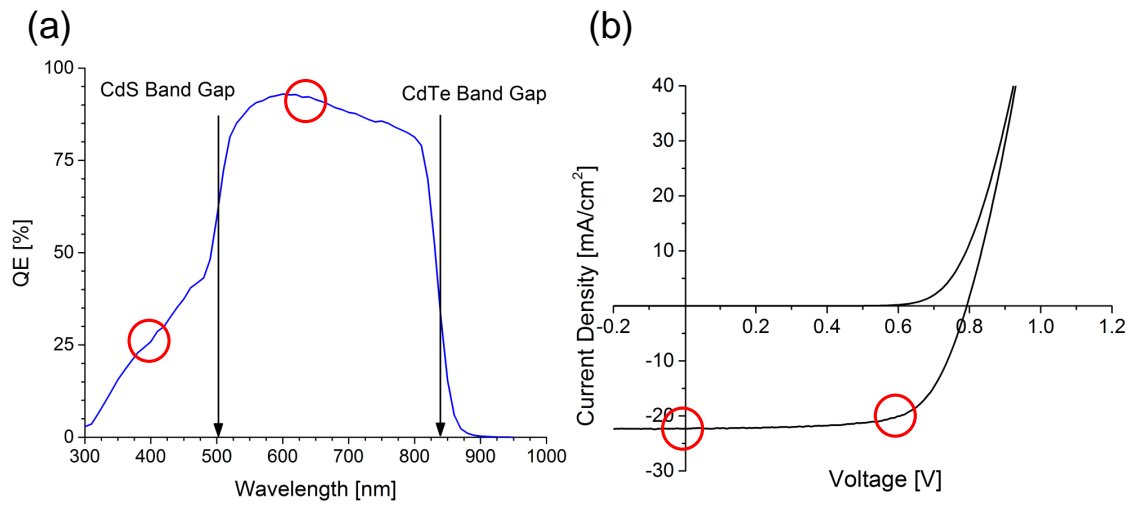


Figure 1.7: (a) QE curve of typical CSU CdTe cell with two wavelengths highlighted used for LBIC measurement and (b) J-V curves of same cell with two possible applied voltage bias points used for LBIC maps presented labeled.

Chapter 2

ELECTROLUMINESCENCE SYSTEM

In this chapter, design, performance and operation details of the electroluminescence (EL) system are discussed. Unless stated otherwise, the EL measurements mentioned in this manuscript were performed with this system.

2.1 Overview of Experimental Setup

The electroluminescence (EL) system built at Colorado State Universities Photovoltaics Laboratory was designed to measure EL radiation from CdTe solar cells and modules of different areas, though it can also be used for other types of cells. The imaging area can vary continuously between 1.4×1.1 cm for cells and 1.3×1.0 m for modules. As discussed elsewhere [14], the system has five major features: light-tight enclosure, cooled-Si CCD detector, imaging lens, current source and a computer; see Fig. 2.1 for a schematic of the setup.

The camera is mounted to a gantry system which can be moved continuously in the x-y plane. The gantry system is mounted to rails along the z-direction and is suspended via a balanced counter-weight system, providing a continuous range of vertical working distance, thus, allowing for any arbitrary imaging area within the limits of the enclosure and imaging lens.

The system was built so that a near-infrared reflection (NIRR) image and an EL image can be collected from the same area. This has an added advantage of overlaying the two images, as some of the defects detected in EL can be more readily identified with a NIRR image. The imaging lens has a magnification ratio of up to approximately 1:1.3, its $4\text{-}\mu\text{m}$ resolution easily resolves details of features as small as $50\ \mu\text{m}$. Although this system was built with the intention of imaging devices of different areas, it typically employs an imaging

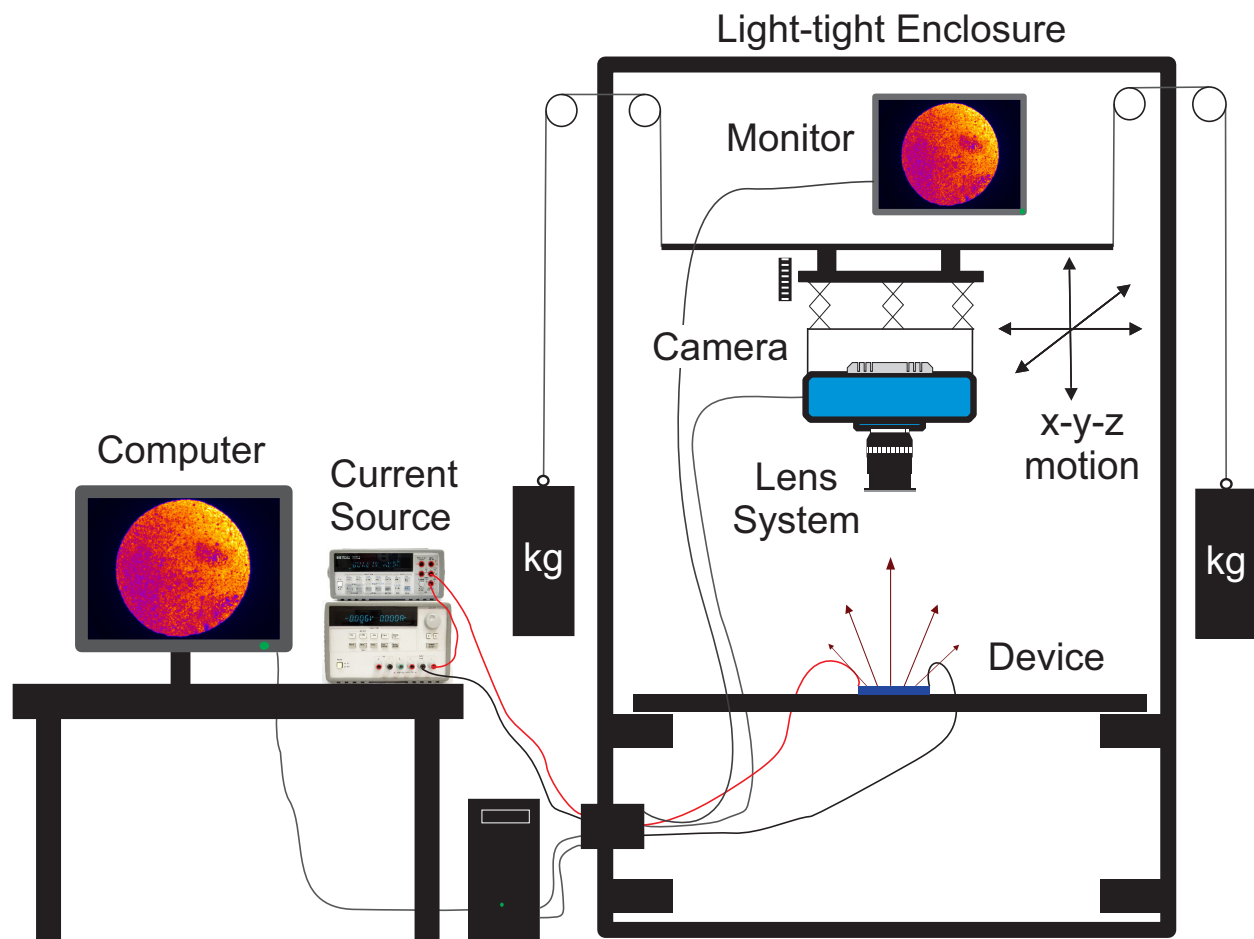


Figure 2.1: Schematic of the EL system with its five main components: light-tight enclosure, camera (detector), imaging lens, current source and computer.

area of 1.4×1.1 cm used to image cells. All further discussions and measurements performed on cells in this manuscript were performed with the macro lens and extension tube.

Open-source software was chosen to operate the camera (Micro-Manager [15]) and for image processing and analysis (ImageJ [16]).

2.2 Detector Array

The detector array is a Peltier-cooled Si-CCD camera composed of 8.3×10^6 pixels (3326×2504 pixels) with each pixel of dimension $5.4 \times 5.4 \mu\text{m}$. When collecting images, the detector is operated at -25°C , since thermal noise would be significant if the detector were to operate at ambient temperature and typical integration times.

The wavelength-response curve of the detector chosen can be found in Fig. 2.2 (black curve), the remaining three curves (blue, green and red) are spectra-response curves for the color version of the detector (not used in the system presented). The EL emission from a CSU CdTe cell is centered about 835 nm, corresponding to a detector response of approximately 25%. Although the system was built to measure EL radiation from CdTe cells, it is also able to measure EL radiation from other cells including smaller-band-gap devices such as CIGS.

The detector employs a 16-bit analog-to-digital converter. After collecting an image, each pixel is of integer value between 0 counts ($2^0 - 1$), corresponding to few photons detected, and 65535 counts ($2^{16} - 1$), corresponding to many photons detected. However, the smallest pixel response in practice is approximately 1275 counts due to a pre-programmed bias level, see Table 2.1 or Fig. 2.7.

Fig. 2.3 is a plot of mean integrated EL intensity from a 850-nm LED as a function of programmed exposure time. The figure demonstrates the linearity of detector holds for a pixel response of up to 5×10^4 counts, far larger than typical EL signals from CdTe cells.

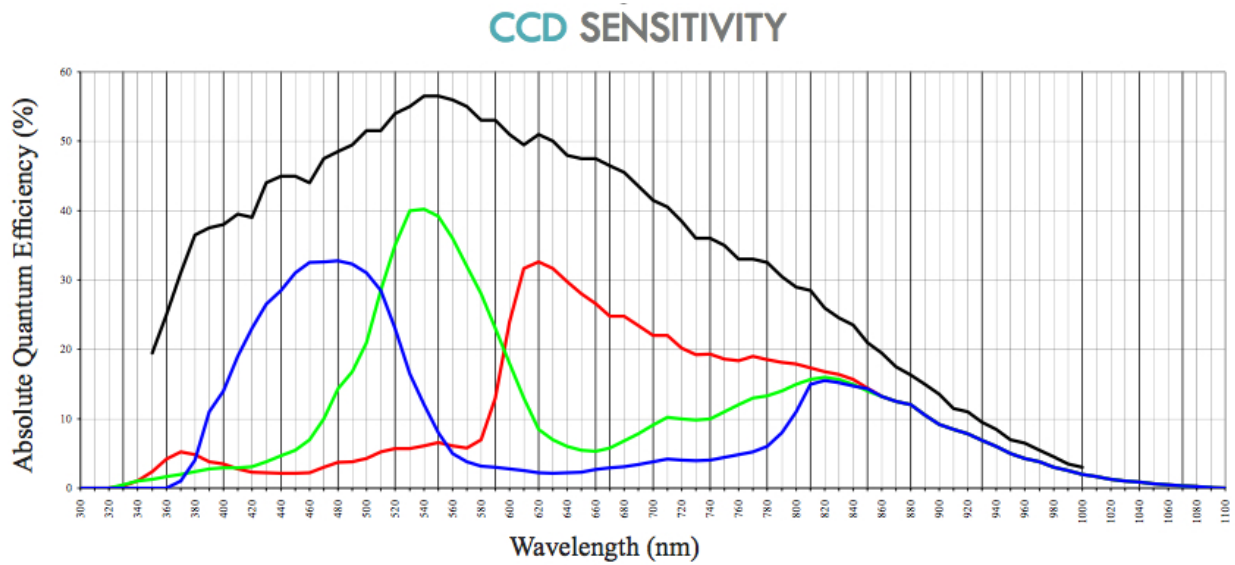


Figure 2.2: Response curve of detector from camera manufacturer (Apogee Imaging Systems). Black curve is for detector used for EL. The response of detector at 835 nm is approximately 25%. The other three curves are for color version of same detector.

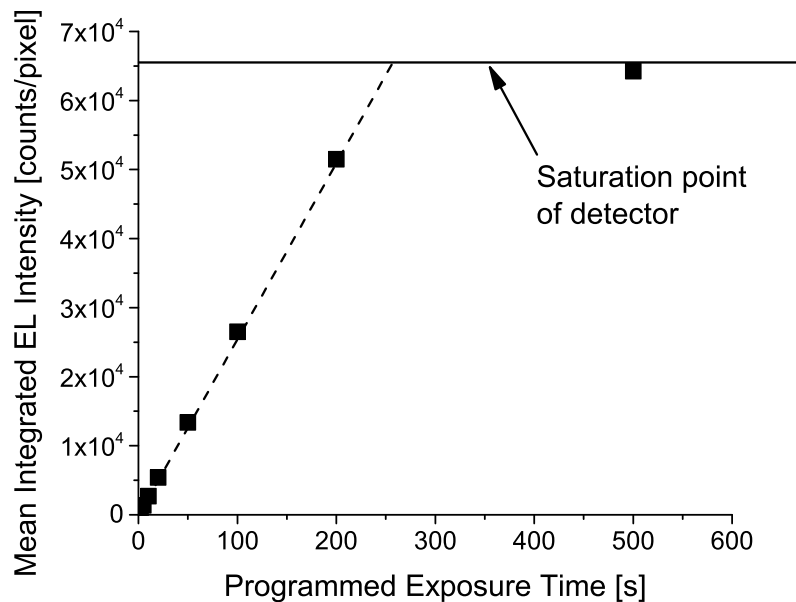


Figure 2.3: Mean integrated pixel response of EL radiation from a 850-nm LED operating in constant current mode as a function of programmed exposure time. Detector is linear up to 5×10^4 counts, far larger than typical signals from CdTe cells.

Table 2.1: Table of specification values for the CCD detector array. Detector array CCD specifications were provided by Apogee Imaging System’s website [17], ”Test Data for CCD” information was provided by the camera manufacturer upon delivery.

CCD Specs	
CCD	Kodak KAF-8300
Array Size	3326×2504 pixels
Pixel Type	16 bit
Pixel Size	$5.4 \times 5.4 \mu\text{m}$
Detector Area	$18 \times 13.5 \text{ mm}$ (243 mm^2)
Detector Diagonal	22.5 mm
Linear Full Well (typical)	2.25×10^4 electrons
Maximum Digitized Well Capacity	4×10^4 electrons
Dynamic Range	64.4 dB
Test Data for CCD	
Gain	0.6 electrons/count
Standard Deviation	14 counts
RMS Noise	9 electrons
Bias Level	1226 counts
120-s Dark Image	1227 counts (includes bias level)
Dark Current	0.01 electrons per pixel per second
CCD Test Temperature	-30°C

2.3 Shutter Speed

The camera chosen for the EL setup utilizes a programmable mechanical shutter which controls the exposure time. At times, it has been advantageous to reduce the exposure time as to avoid saturating the detector. To test the precision of the mechanical shutter timing, EL image were collected of an LED operating in constant current mode at different programmed exposure times. If the precision of the shutter were perfect, one would expect a graph of EL intensity vs exposure time to have an intercept of 0.

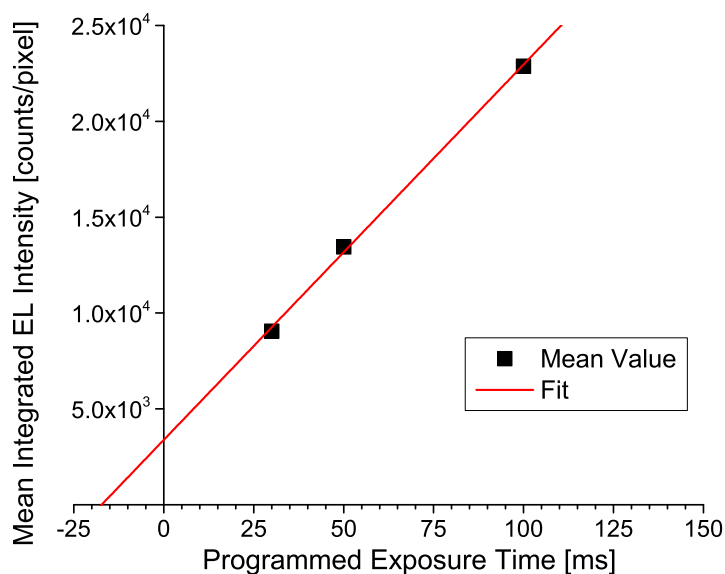


Figure 2.4: Mean integrated EL intensity as a function of programmed exposure time for a LED operating in constant current mode to test the precision of the programmed shutter exposure time. The offset in the x-axis corresponds to an offset in the programmed exposure time of 17 ms.

Fig. 2.4 is a plot of EL intensity as a function of programmed exposure time of the 850 nm LED operating in constant current mode of programmed exposure times 30, 50 and 100 ms. The fit for the data points has an offset of approximately 17 ms, corresponding to the imprecise nature of a mechanical shutter, which is open for 17 ms more than the programmed value. However, this time delay is only corrected for programmed exposure times of 10^3 ms or less.

2.4 Optics

The EL system has two primary imaging lenses: a micro lens for imaging large areas such as modules and a macro lens for imaging small areas such as cells or selected defect areas in modules. The micro lens is a 24-mm Nikon brand lens with an f-stop of f/2.8. The macro imaging lens is a Carl Zeiss brand lens with focal length of 50 mm and an f-stop of f/2.0. Both lenses are typically used with a 720-nm long-pass optical filter to reduce background light and to improve focusing in the NIR; see transmittance plot in Fig. 2.5. An extension tube of length 45 mm is mounted between the imaging lens and the camera body to increase magnification, resulting in a magnification ratio of approximately 1:1.3 (ratio of image height to object height is approximately 1.3). Even though this system was built with the intention of imaging devices of vastly different areas, it has most often been used to image cells. All further discussions and measurements in this manuscript employed the Carl Zeiss macro lens and extension tube with the exception of the discussion of module defects in Ch. 5.

As a result of utilizing a large aperture and an extension tube, the depth of focus is significantly reduced to approximately $\pm 200 \mu\text{m}$, which makes the optical lab-jack shown in Fig. 2.1 an imperative component for a well-focused image. This feature has a significant side-benefit in that a near-constant working distance implies an effectively constant absolute calibration of pixel size and response, thus, images collected on different days may be compared with confidence.

Certain lenses can exhibit artifacts known as vignetting where the recorded image, especially near the edges, may not reflect the full light intensity. The degree to which this artifact effects the resulting image was explored for the Carl Zeiss lens with extension tube and discussed further in the following section.

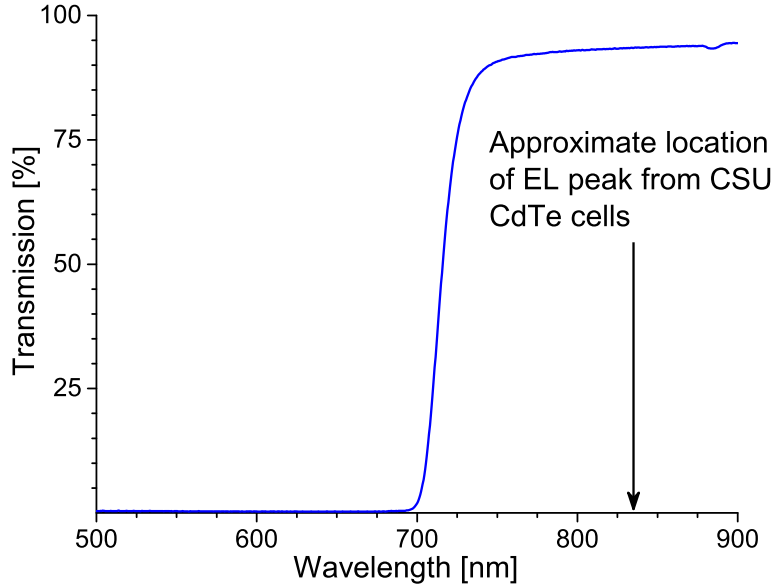


Figure 2.5: Transmission plot of optical filter for EL system with approximate location of CSU CdTe EL emission peak labeled.

2.5 Image Correction

Images collected by the detector may not be a true mapping of the EL intensity emitted from the cell due to several factors such as: vignetting of the lens, variations in the pixel-to-pixel response, imperfections with the imaging optics, or contaminants on any one of the optical elements. It is expected that of these artifacts, vignetting is most detrimental. Vignetting is the clipping of light rays in the optical assembly, resulting in non-uniform attenuation of the light. Fig. 2.6 is an optical image of a uniform light source, with false coloring applied and normalized to unity with \log_{10} scale, demonstrating the vignetting effect. Typical CSU CdTe cells have a diameter of approximately 1 cm and are manually centered in imaging area, attenuation of the signal is maximum at the cell edge and is approximately 20%. Other than background subtraction, correction factors for EL images, as described elsewhere [18], were not taken into account as the graphs and images are displayed on a log-scale where other corrections would be small.

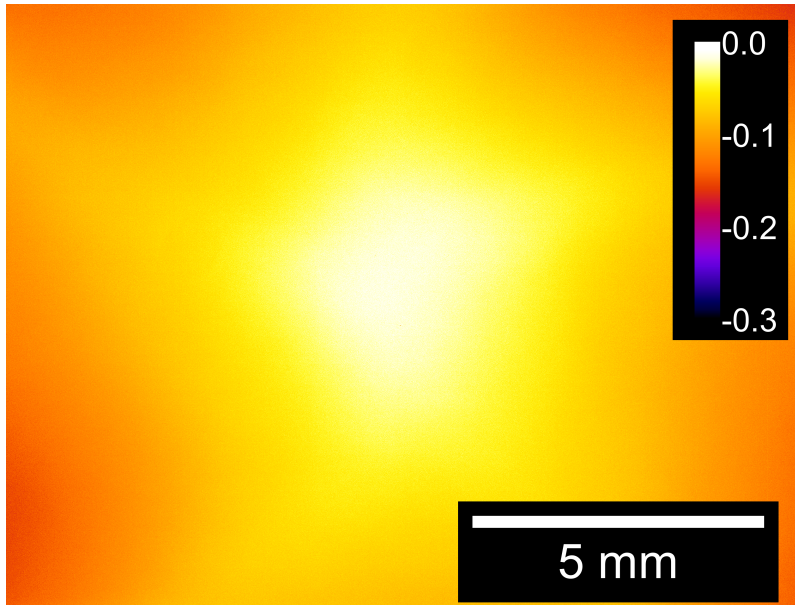


Figure 2.6: Image of uniform light source, normalized to maximum pixel response with a \log_{10} scale. Typical CSU CdTe cells (~ 1 cm in diameter) can have as much as a 20% reduction in signal at cell edge.

2.6 Background Levels

Reduction of background noise is critical in collecting high-quality EL images as solar cells are often inefficient at converting injected electrons into emitted photons ($10^{-4}\%$ for CdTe cells [12]). Some sources of background noise include: stray light, thermal noise in the detector and readout noise from the electronics in the camera.

The light-tight enclosure coupled with the 720-nm long-pass filter and background-image subtraction mitigate stray light, while operating the detector at -25°C sufficiently reduces thermal noise. In this section, the readout noise from the detector is investigated.

Background images were collected at various exposure times (10^3 , 2×10^3 , 4×10^3 , 10^4 , 2×10^4 , 4×10^4 and 10^5 ms), ten images were collected at each exposure time. Each set of 10 images was consolidated into 2 images: an image of mean pixel response and an image of standard deviations. The image of the standard deviations is the calculated standard deviation at each pixel location for all 8.3×10^6 pixels and all 10 images; the same is true for

the image of mean pixel response. Fig. 2.7 is a plot of the mean of each of the two images (mean pixel response and standard deviations) plotted against programmed exposure time. The mean pixel response increases by approximately 3 counts yet the integration time has increased by two decades, in agreement with the CCD test data for the dark current in Table 2.1.

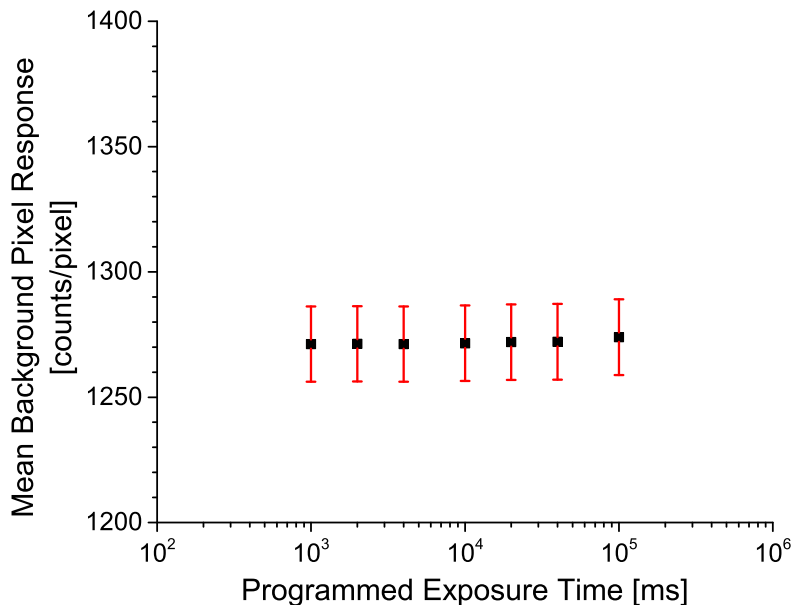


Figure 2.7: Mean pixel response with its respective standard deviation of data of background levels as a function of exposure times with the detector array operating at -25°C . The standard deviation in background levels is significantly smaller than typical EL signals of $10^3 - 10^4$ counts.

Typical EL signals from moderately efficient solar cells are on the order of $10^3 - 10^4$ counts above background level, far larger than the standard deviations seen in Fig. 2.7. The noise in the detector is sufficiently small and for practical purposes, independent of exposure time. Thus, when collecting an EL image, the systems signal-to-noise ratio increases linearly with exposure time. It should be noted that the signal-to-noise ratio only behaves linearly for a finite range of exposure times as the pixel response eventually saturates, see Fig. 2.3.

2.7 Calibration

Although there exists different factors for calibration of the system [19], only two spatially homogenous factors were considered for calibration of detector array operating at a fixed temperature (see Table 2.2): pixel size and pixel response. As discussed in Sect. 2.4, the working distance of the system for most measurements is nearly constant, resulting in an effectively constant value for absolute calibration of pixel size and pixel response.

2.7.1 Absolute Calibration of Pixel Size

The absolute calibration of pixel size, ϵ , has been explored through different experimental avenues, all of which have resulted a consistent answer of approximately 243 pixels/mm.

An image of a commercially available 150- μm diameter spatial filter with light entering its aperture was collected and used to confirm absolute calibration of pixel size. The pixel size in the image was then calibrated to the accepted value of 243 pixels/mm and a line cut across the aperture was then performed. Fig. 2.8 is a graph of the line cut across the 150- μm aperture with a scale of length 150 μm placed at half-maximum intensity. The scale spans the entire width of the curve, acting as an independent verification of the absolute calibration of pixel size.

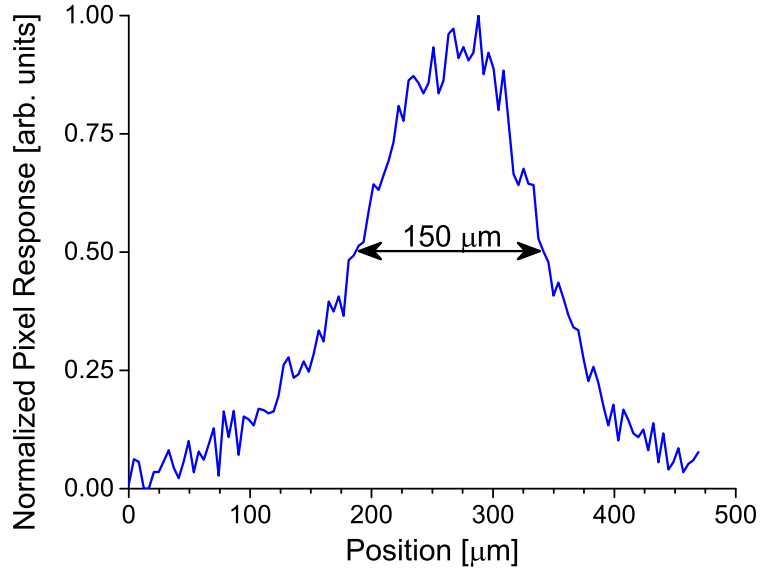


Figure 2.8: Line cut from image of aperture of diameter $150 \mu\text{m}$ under illumination. Scale drawn at half-max has length of $150 \mu\text{m}$.

2.7.2 Calibration of Pixel Response

A commercially available AlGaAs LED (part number LED851W from ThorLABS) was used to calibrate the EL system. This LED is packaged in a T0-18 can, encapsulating the diode in a optically transparent window material. It has a peak emission centered at 850 nm (see Fig. 2.9) with a nominal optical power output of 8 mW when operating with a forward injection current of 20 mA, Fig. 2.10 is an EL image of the LED.

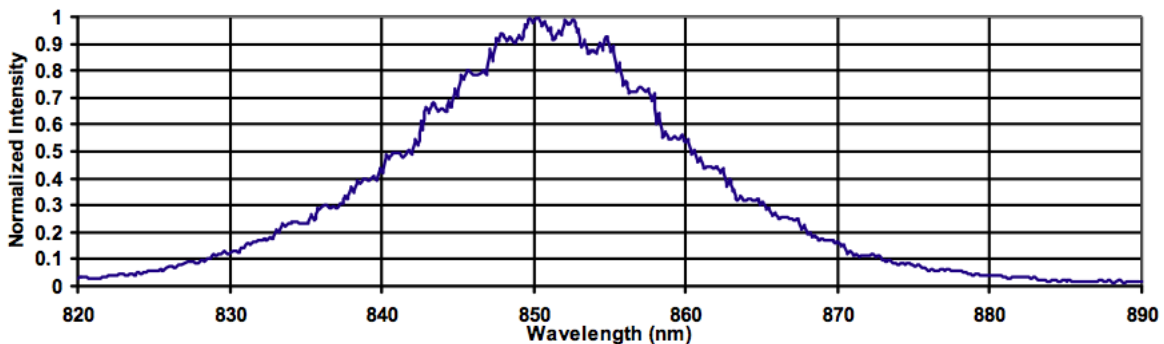


Figure 2.9: Typical EL spectrum from 850 nm LED. Data is from manufacturers website.

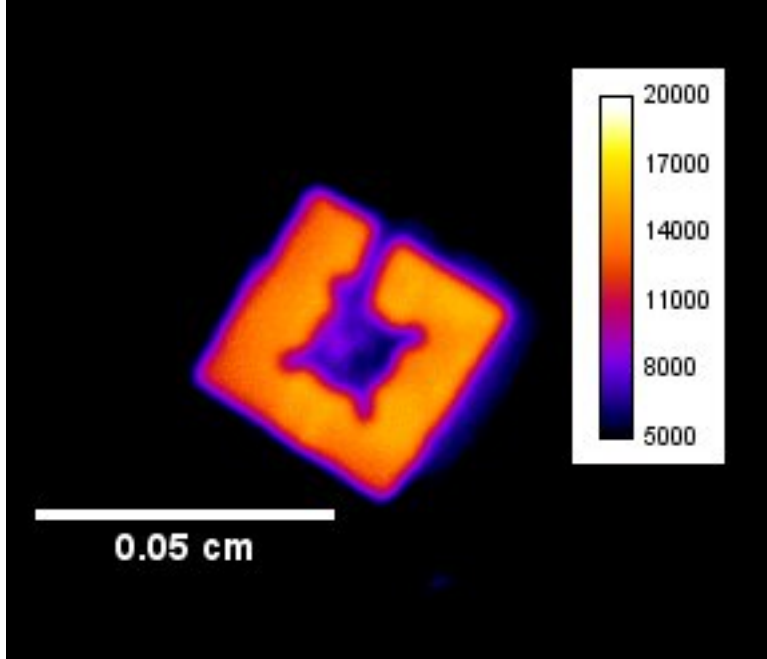


Figure 2.10: EL image of 850 nm LED used for absolute calibration of EL system.

This LED will saturate the detector when operating at its standard injection current. To reduce the signal from the LED, a neutral density filter was therefore inserted in the beam path along with reduced exposure time, injection current, and aperture area.

The calibration of the pixel response for the EL system was achieved by measuring the EL intensity of the LED with a given optical power with a given injection current. Fig. 2.11(a) is of mean pixel response as a function of current through diode and Fig. 2.11(b) mean pixel response (corrected for attenuation) from Fig. 2.11(a) as a function of calculated photon flux. This curve is known to be non-linear for low voltage biases. The higher-voltage bias regime where the curve is linear was used for fitting.

The inverse slope in Fig. 2.11(b), δ with units of photons/count, is the calibration parameter that relates pixel counts to the number of photons of wavelength 850 nm emitted from the device. Of note, δ is expected to have a modest wavelength dependence, since both the detector response and the transmittance of the optical elements will vary with wavelength. Nevertheless, for solar cells with band gaps similar to CdTe and AlGaAs, it should be considered reasonably accurate. It should be noted that the specifics listed here were intended

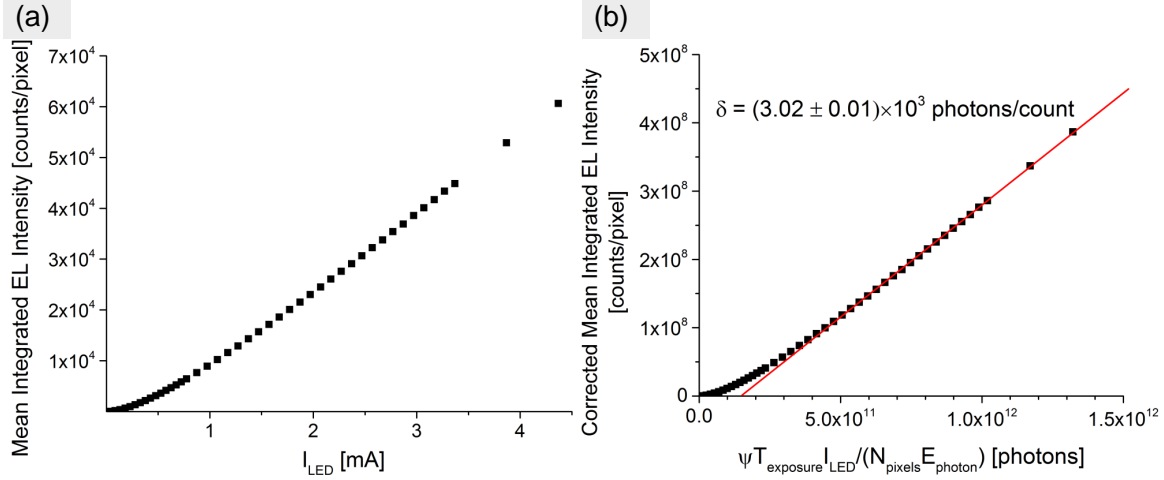


Figure 2.11: (a) mean integrated EL intensity of LED as a function of LED injection current, (b) calculated mean pixel value, corrected for attenuation as a function of emitted photons, calculated from (a).

as a rough calibration and that a more accurate calibration should employ this technique with a more accurately calibrated illumination source.

The pixel response parameter, δ , from Fig. 2.11(b) can be expressed in its analytical form as Eq. 2.1 below,

$$\delta = \frac{\psi \cdot t_{exposure}}{N_{pixels} \cdot E_{photon}} \frac{dI_{LED}}{d\phi}, \quad (2.1)$$

where, $t_{exposure}$ is the image exposure time, ψ is the fraction of optical output power of known photon energy at known injection current (approximate value provided by the manufacturer), E_{photon} is the peak LED photon energy, I_{LED} is the current through the LED and ϕ is the mean pixel response. Eq. 2.1 is especially useful in calculating the external quantum efficiency of a solar cell in an LED mode (EQE_{LED}) in dimensionless units from an EL image as described by Eq. 2.2 below,

$$EQE_{LED} = \frac{\delta}{e \cdot \epsilon^2} \left[\frac{\text{C} \cdot \text{photons} \cdot \text{pixel}}{\text{electron} \cdot \text{counts} \cdot \text{cm}^2} \right] \cdot \left(\frac{\Phi}{J \cdot t_{exposure}} \right) \left[\frac{\text{counts} \cdot \text{cm}^2}{\text{A} \cdot \text{s} \cdot \text{pixel}} \right], \quad (2.2)$$

where, δ is the calibration of pixel response calculated from Eq. 2.1, e is the elementary charge, ϵ is the calibrated pixel size, Φ is the mean pixel counts from the EL image, J is the injection current density, and $t_{exposure}$ is the exposure time of EL image.

Throughout this manuscript, EL intensity is normalized to exposure time and current density, $\frac{\Phi}{J \cdot t_{exposure}}$, which as demonstrated by Eq. 2.2 is directly proportional to EQE_{LED} . The maximum theoretical value for EQE_{LED} is unity, which places an upper limit on $\frac{\delta}{e \cdot \epsilon^2}$ to be approximately $6 \times 10^{-10} \left[\frac{\text{C} \cdot \text{photons} \cdot \text{pixel}}{\text{electron} \cdot \text{counts} \cdot \text{cm}^2} \right]$. Although this technique can be an adequate method for calibration of pixel response, a different approach to calibration of the EL system will be discussed in a later section.

2.8 Experimental Details

The process of collecting an EL image is separated into 4 steps: focusing of the camera, collecting a NIRR image, collecting a background EL image, and collecting an EL image. The camera's programmed settings for each of the four steps is presented in Table 2.2.

Cells are mounted on a custom cell mount, with spring-loaded pogo pins for electrical contacting. Although there are 4 pogo pins for contacting the TCO, there is only one pogo pin for the back contact, which helps flag any issues with back-contact series resistance. The cells' orientation in the images presented are preserved so that defect regions identified with EL can be correlated with other information such as a non-uniform temperature profile of the substrate during material processing.

Prior to collecting EL images, the camera must be focused, which is accomplished by adjustment of the working distance. Coarse adjustment is achieved by manually moving the gantry system (attached to a counter-weight system), while fine adjustment is achieved by an optical lab-jack (360° rotation of knob corresponds to an average displacement of $\simeq 0.7$ mm) mounted to the camera. Meanwhile, a 150-W halogen bulb coupled to an optical fiber is used to illuminate the cell (not depicted in Fig. 2.1). A 720-nm long-pass filter mounted to the camera lens is employed as to improve focusing in the near infrared (NIR) (peak EL emission for CdTe cells is centered about 835 nm).

Once the cell is in focus, the doors of the enclosure are closed and a NIR reflection (NIRR) image is collected. NIRR images can be helpful as sub-band gap light is useful when identifying defects which exist in the back of the cell (such as the back-contact). The advantage of a NIRR image is illustrated in Ch. 4, where identification of defects in cells are discussed.

Table 2.2: Table of typical values used while the camera is in one of four states: focusing the image, collecting a NIRR image, collecting a background EL image and collecting an EL image.

Camera Settings				
Property	Focusing	NIRR Image	Background EL Image	EL Image
CCD Temperature [°C]	-25	-25	-25	-25
Exposure Time [ms]	30	10^3	10^5	10^5
J [mA/cm ²]	0	0	0	40
Pixel Type	12 bit	16 bit	16 bit	16 bit
External Illumination	on	on	off	off

Following the collection of a NIRR image, the external illumination source is turned off, and there is no intentional background light within the enclosure. A background image may now be collected, followed by an EL image of a cell after the current source is properly adjusted. The power supply used is a 30-W Agilent E3611A analog DC current source in series with a HP34401A digital multimeter for current monitoring. Post-processing of the three collected images is discussed in the following section.

2.9 Image Processing

Image processing was performed with the ImageJ open-source software package [16]. Some of the image processing capabilities include: background-image subtraction, change of

pixel type (16 bit to 32 bit), mathematical operations such as taking the log of an image, generation of histograms or line cuts of select regions, and application of false coloring to an image.

Native formats of collected images are of 16-bit format and need be converted to 32-bit format since 32-bit pixels are of most value, while 16-bit pixels are restricted to integer values. Otherwise, ImageJ would truncate the pixel value after performing mathematical operations such as taking the log.

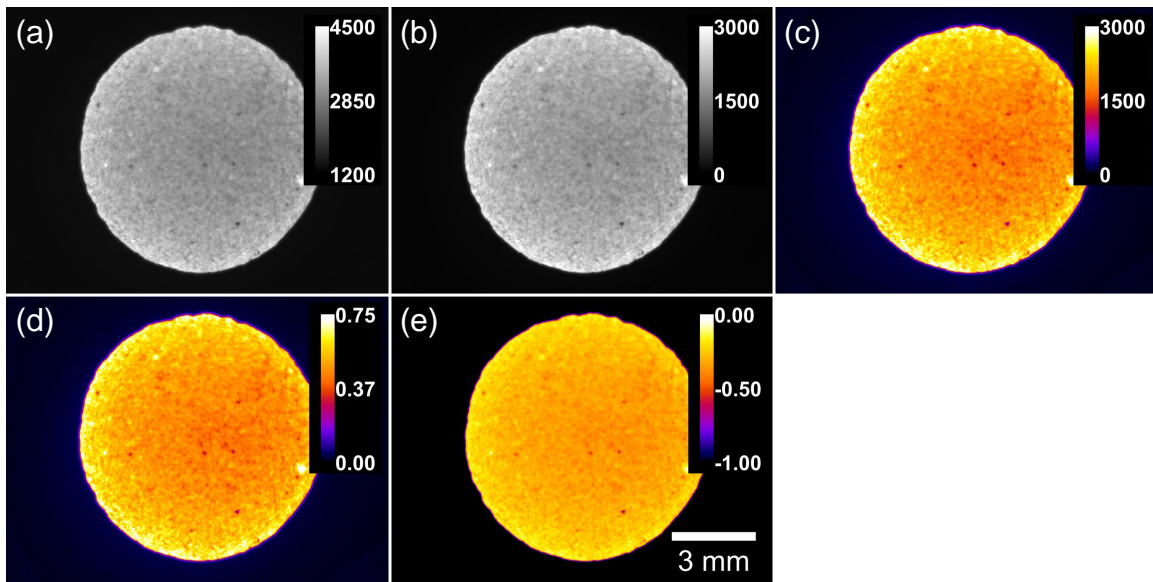


Figure 2.12: Subsequent EL image manipulation of a cell using ImageJ: (a) raw image, (b) raw image after background-image subtraction, (c) false coloring applied, (d) image normalized to current density and exposure time and finally (e) image with \log_{10} scale.

Fig. 2.12 is an EL image of a typical CSU CdTe cell during various steps of processing. Intensity bars are placed on images to illustrate mathematical operations performed between steps. Fig. 2.12(a) is of raw EL image, (b) post-background image subtraction, (c) application of false coloring, (d) normalization of image to exposure time and injection-current density (typically $4000 \text{ mA}\cdot\text{s}/\text{cm}^2$) and (e) image with \log_{10} scale.

2.9.1 Look-Up Table

A reference table used to map pixel response to a color is known as a Look-Up Table (LUT). Specific LUTs mentioned in this manuscript are as defined by ImageJ. LUT's serve as a means to improve contrast of an image and only two different LUT's are used in this manuscript: Gray and Fire. Examples of these LUTs can be seen in Fig. 2.12(b) and Fig. 2.12(c), respectively. A LUT may be inverted (bright spots appear dark and visa versa) to improve contrast. However, this has only been done for the NIRR images.

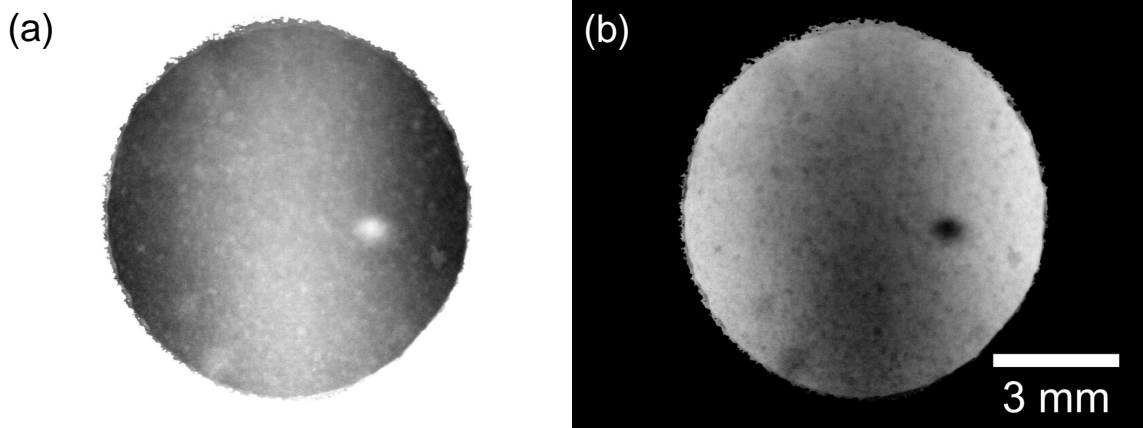


Figure 2.13: Typical NIRR image with Gray LUT (a) and inverted Gray LUT (b). Inverted LUT can improve visibility of defects seen in NIRR image.

Fig. 2.13 is a NIRR image of the typical CSU CdTe cell as presented in Fig. 2.12 with a standard Gray LUT (a) and an inverted Gray LUT (b). Lower-contrast defects can be more readily seen in (b).

2.10 Calculating Area From Electroluminescence Image

Due to the high spatial density of pixels in the detector array, images can be an effective tool for calculating areas such as the luminescent area of a cell. Fig. 2.12(d) is an EL image of the cell used to calculate luminescent area, which should be very similar to the active area of the solar cell.

One may calculate the cell luminescent area by first calculating the area projected onto the detector array and scaling it with the absolute calibrated pixel area, as expressed in Eq. 2.3 below,

$$\text{Area}(P_{min}) = \frac{1}{\epsilon^2} \sum_{P_{min}}^{\infty} H(P) \quad (2.3)$$

Where, ϵ is the absolute calibrated pixel size, P_{min} is the minimum pixel response used for the summation and $H(P)$ is the histogram of select region from EL image. The summation limits are from P_{min} to ∞ , since the pixels of large response are from the luminescing cell and it's only the lower-limit of pixel response which is in question. Fig. 2.14 is a plot of Eq. 2.3 as a function of P_{min} , which can be estimated from a line cut taken of the EL image and is plotted in Fig. 2.15. A minimum pixel response of 0.16 counts·cm²/s·mA·pixel was found from a histogram generated from just-within the cell's luminescent area. Cell's area of 0.625 ± 0.012 cm² was calculated from a minimum pixel response subjectively chosen to be 0.1 counts·cm²/s·mA·pixel, in agreement with value deduced from an existing area meter.

This technique is able to readily identify the area of a luminescent object and the uncertainty on the measured value of a well-behaved cell is approximately $\pm 2\%$ due to the uncertainty in ϵ . However, this technique can be inaccurate as a cell may exhibit non-luminescing areas within the active area of the device, and thus those areas would not be accounted for with this technique, for example the cells depicted in Fig. 4.3(a).

Note that the same may be done for images where one is only interested in calculating the area of a masked object. For example, a transmission image of a solar cell using sub-band-gap light can be used to quickly, accurately, and precisely measure the shadowed area of a cell's metal back-contact, as discussed elsewhere [4]. In which case, Eq. 2.3 needs to be modified as P_{min} is well-defined ($P_{min} = 0$) and P_{max} needs to be determined.

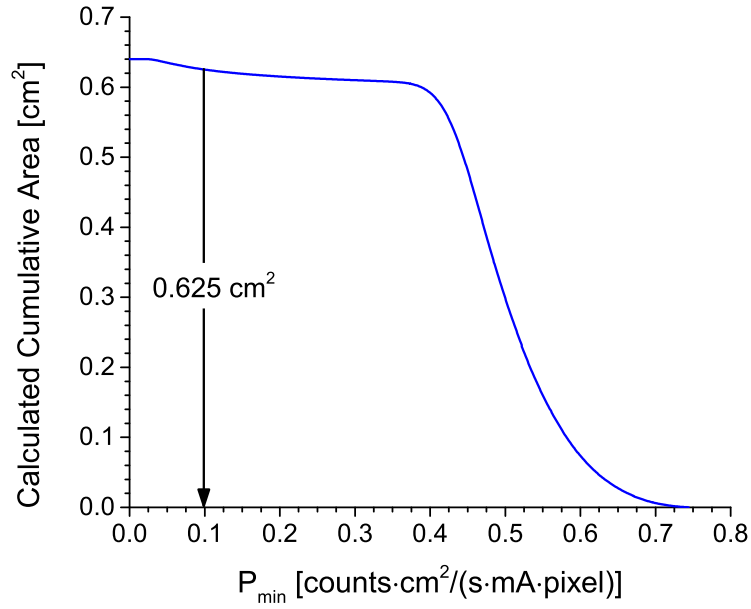


Figure 2.14: Area of cell as a function of minimum pixel response (P_{min}), as analytically demonstrated in Eq. 2.3. A luminescent area of 0.625 cm^2 was deduced from a P_{min} of $0.1 \text{ counts}\cdot\text{cm}^2/(\text{s}\cdot\text{mA}\cdot\text{pixel})$, chosen from line scribe of cell in Fig. 2.15 and histogram from area within cell (not shown).

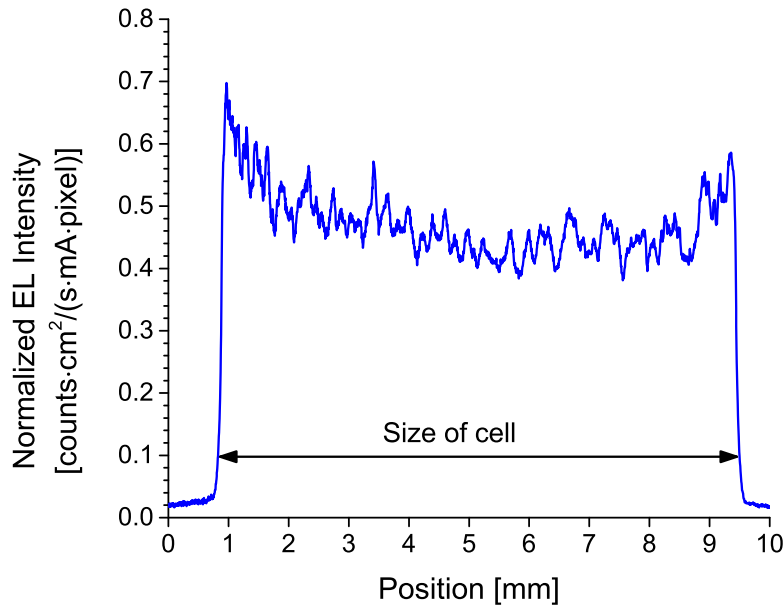


Figure 2.15: Line scribe from EL image of cell in Fig. 2.12(d) used to estimate P_{min} for calculation of cell luminescent area in Fig. 2.14

Chapter 3

EL INTENSITY AND ITS RELATIONSHIP TO CELL VOLTAGE

A cell operating in forward electrical bias in the dark will act as a power consumer with some fraction of that energy converted to light (radiative efficiency) and the remainder into heat. As discussed by Rau and others [20, 21] as a cell's radiative efficiency (EQE_{LED}) improves, so too should the cell's open-circuit voltage until it realizes its maximum theoretical value, at which point the radiative efficiency will become unity [20].

In this chapter, the $EQE_{LED} - V_{OC}$ relationship is investigated for a large number of thin-film polycrystalline CdTe cells, a crystalline GaAs reference cell, and the AlGaAs LED discussed in Sect. 2.7.2. The CdTe cells were made at CSU, Abound Solar, and First Solar. CdTe samples manufactured at CSU and Abound Solar were fabricated with a close-space-sublimation (CSS) technique. The spectrum of CdTe cells used for this study include vastly different manufacturing recipes such as various window layers [22], window layer film thickness, Cl passivation treatment, alloyed absorber layers (modified band gap), and devices with a back-contact barrier. The CdTe devices presented here cover a range of photovoltaic conversion efficiencies from 10% to 19%. The crystalline GaAs cell has an efficiency of 18%, and the AlGaAs LED an efficiency of $\sim 3\%$. The devices studied have a diode ideality factor between 1.6 and 2.0, calculated from their light J-V curves. Samples were measured under standard measurement conditions. Open-circuit voltages used were measured immediately prior to the applied voltage bias sweep to mitigate any thermal effects. The EQE_{LED} of devices of different absorber materials can vary by many decades, as shown by Green [12] and Raguse [23]. Consequently, measurement conditions for the GaAs and AlGaAs devices were performed at a reduced exposure time of 100 ms. All CSU and Abound polycrystalline CdTe cells were measured with an injection current density of 40 mA/cm^2 and an exposure time of 100 s.

EL intensities listed in this chapter are the mean integrated EL intensity normalized to injection current density and exposure time (proportional to EQE_{LED}) and are referred as "normalized EL intensity" throughout.

For selected cells, temperature dependent EQE_{LED} was investigated and failure of the $EQE_{LED} - V_{OC}$ relationship is discussed as well as the mathematical framework underlying this theory.

3.1 Open-Circuit Voltage Correction Offset

Others have explored the $EL - V_{OC}$ relationship for devices of similar absorber material [14, 24] and have shown the relationship to be exponential. In this section, normalized EL intensity for various samples are plotted as a function of open-circuit voltage to illustrate the necessity of an open-circuit voltage offset.

Fig. 3.1 is a plot of devices normalized EL intensity as a function of decreasing measured open-circuit voltage. The line drawn has an inverse slope of -26 mV and is a fit for only the CSU and Abound Solar cells, which have an absorber band gap very close to the accepted CdTe value.

As illustrated in Fig. 3.1, devices of a single band gap will fall on the trend line. However, when compared to devices of a different band gap, one no longer expects agreement. A voltage offset is required which takes into account devices opto-electronic properties such as band gap and short circuit current density. In the following section, EQE_{LED} will be derived and in doing so, the appropriate voltage offset will be calculated.

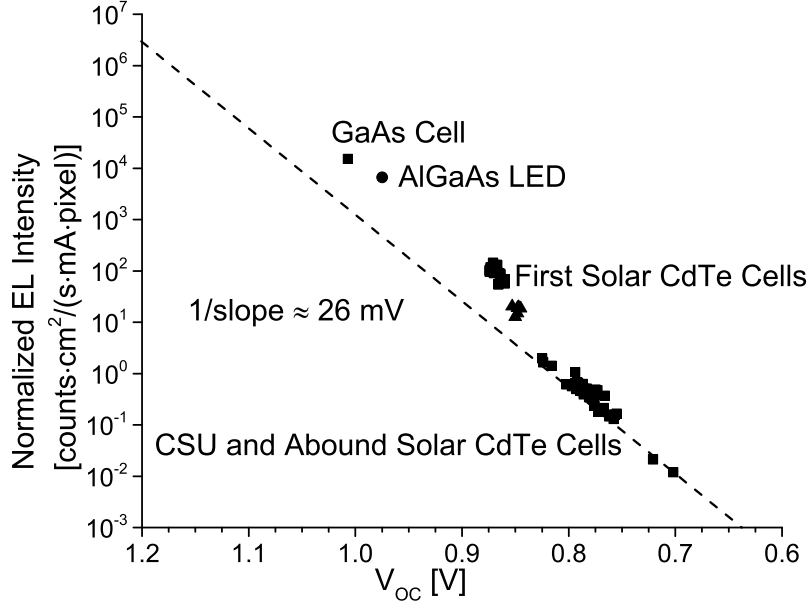


Figure 3.1: Plot of EL intensity as a function of decreasing open-circuit voltage. Fit above is for CSU and Abound Solar cells only. Deviations suggest variations in band gap.

3.2 Derivation of External Quantum Efficiency of an LED

The characteristic diode equation for a well-behaved device, described by Eq. 1.3, may be solved for open-circuit conditions,

$$V_{OC} = \frac{Ak_bT}{q} \ln\left(\frac{J_{SC}}{J_0}\right) \quad (3.1)$$

Although V_{OC} depends on four parameters in Eq. 3.1, the saturation current density, J_0 , is generally the most critical. Rau theorized that the limiting factor of saturation current density of a solar cell should be equal to the absorption of a cell with light incident on it from a black body whose temperature is equal to the cell's [20], as written in Eq. 3.2 and Eq. 3.3 below. This definition is equal to the Shockley-Queisser approach when a cell's QE is unity for photon energy greater than the band gap and zero for photon energy less than the band gap [21].

$$J_{0,ideal} = q \int_0^\infty QE(E) \Phi_{bb}(E, T) dE \quad (3.2)$$

$$\approx \frac{2\pi q}{h^3 c^2} \int_{E_{gap}}^{\infty} E^2 e^{-\frac{E}{k_b T}} dE$$

$$J_{0,ideal} \approx \frac{2\pi q}{h^3 c^2} e^{-\frac{E_{gap}}{k_b T}} [E_{gap}^2 k_b T + 2E_{gap}(k_b T)^2 + 2(k_b T)^3], \quad (3.3)$$

where $\Phi_{bb}(E, T)$ is Planck's black body distribution, h is Planck's constant, c is the speed of light in a vacuum, E_{gap} is the cell's energy gap and $k_b T$ is the thermal energy.

One can calculate the characteristic diode equation for an ideal cell for a given QE curve in the absence of non-radiative recombination by substitution of the saturation current density found in Eq. 1.3 with the ideal saturation current density, and setting the diode ideality factor to unity [11, 20],

$$J_{rad} = J_{0,ideal}(e^{\frac{qV}{k_b T}} - 1) - J_{SC} \quad (3.4)$$

Solving the above equation under open circuit conditions yields the ideal open-circuit voltage of a cell in the absence of non-radiative recombination,

$$V_{OC}^{RAD} = \frac{k_b T}{q} \ln\left(\frac{J_{SC}}{J_{0,ideal}}\right) \quad (3.5)$$

The External Quantum Efficiency of an LED (EQE_{LED}) is a useful metric to evaluate the quality of an LED. It is defined as the fraction of injected carriers which recombine radiatively (J_{rad}), with the resulting photon emitted from the device to the total number of injected carriers ($J_{rad} + J_{non-rad}$)[11, 20],

$$EQE_{LED} = \frac{J_{rad}}{J_{rad} + J_{non-rad}} = \frac{J_{rad}}{J_{total}} \quad (3.6)$$

Eq. 3.4 can be substituted for J_{rad} with a given QE curve equal to that of the cell in question, and Eq. 1.3, which has equivalent parameters to the cell in question, can be substituted for J_{total} , under no light bias, into Eq. 3.6,

$$EQE_{LED} = \frac{J_{0,ideal}(e^{\frac{qV}{k_b T}} - 1)}{J_0(e^{\frac{qV}{k_b T}} - 1)} \quad (3.7)$$

Substituting the integral form of $J_{0,ideal}$, Eq. 3.2, in the above equation and evaluating it at the measured open-circuit voltage (V_{OC}) of a cell with the assumption that superposition of the J-V curve holds (a shift in the dark J-V curve is equal to the light J-V curve), eliminating EQE_{LED} 's dependence on diode ideality factor of measured cell,

$$EQE_{LED} = qe^{\frac{qV_{OC}}{k_bT}} \frac{\int_0^\infty QE(E)\Phi_{bb}(E,T)dE}{J_{SC}} \quad (3.8)$$

substituting the definition for J_{SC} from Eq. 1.5,

$$EQE_{LED} = e^{\frac{qV_{OC}}{k_bT}} \frac{\int_0^\infty QE(E)\Phi_{bb}(E,T)dE}{\int_0^\infty QE(E)AM1.5(E)dE} \quad (3.9)$$

Note the importance of the relationship in Eq. 3.9 above; EQE_{LED} may be calculated of any device with knowledge of the device temperature, the measured QE curve, and the open-circuit voltage. This relationship has been explored by others [12], and their indirect measurement of EQE_{LED} is compared the direct measurement of EQE_{LED} performed by [13] and to the relative measurement of EQE_{LED} performed in this manuscript. The respective data points are plotted together in the following section.

Taking the natural log of both sides of Eq. 3.9 and substituting Eq. 3.5 yields,

$$\boxed{\ln(EQE_{LED}) = -\frac{q}{k_bT}(V_{OC}^{RAD} - V_{OC})} \quad (3.10)$$

Which demonstrates a powerful relationship between the efficiency of a device operating as an LED and its voltage deficit (i.e., difference between ideal open-circuit voltage and the measured open-circuit voltage of a solar cell).

3.3 Results

Calculation of the voltage deficit values ($V_{OC}^{RAD} - V_{OC}$) for the devices shown in Fig. 3.2 as well as devices presented elsewhere [12, 13] is presented in Table 3.1. Of the devices measured at CSU, except for the AlGaAs LED, QE measurements were used to calculate device band gap as described in Sect. 1.4.4. The V_{OC}^{RAD} values were either calculated using

Eq. 3.3 and measured short-circuit current density or provided in literature and confirmed using Eq. 3.3 whenever possible.

Fig. 3.2 re-plots the data in Fig. 3.1 as a function of voltage deficit rather than the open-circuit voltage. It clearly demonstrates that when differences in band gap, and to a lesser extent, differences in short-circuit current density are taken into account, all the data falls on a single line with a negative inverse slope approximately equal to k_bT/q .

Table 3.1: Table of V_{OC}^{RAD} values for devices of different band gaps and current densities. Tabulated values were calculated at room temperature and their energy gap was estimated from technique discussed in Sect. 1.4.4 and V_{OC}^{RAD} values were either calculated using Eq. 3.3 or provided in publication.

Device	Energy Gap [eV]	J_{SC} [mA/cm ²]	$V_{OC}^{RAD} - V_{OC}$ [V]	EQE_{LED} [photons/electron]
GaAs [12]	1.415	30	0.043	2×10^{-1}
GaAs	1.415	25	0.138	7×10^{-3}
AlGaAs LED	1.460	3	0.158	3×10^{-3}
c-Si [13]	1.12	37	0.185	1×10^{-3}
CIGS [13]	1.21	31	0.207	3×10^{-4}
CdTe (First Solar)	1.400	30	0.262	7×10^{-5}
CdTe (CSU)	1.485	23	0.414	3×10^{-7}
CdTe (Abound Solar)	1.485	23	0.509	6×10^{-9}

Fig. 3.3 is a plot of EQE_{LED} as a function of voltage deficit. Calibration of normalized EL intensity (pixel response) was achieved by plotting cells of directly measured EQE_{LED} from T. Kirchartz [13], calculated EQE_{LED} using Eq. 3.9 from M. Green [12], and overlaying the data points found in Fig. 3.2. In agreement with theory, the intercept is very near unity in spite of different calibration techniques used. This expands the EQE_{LED} -voltage deficit

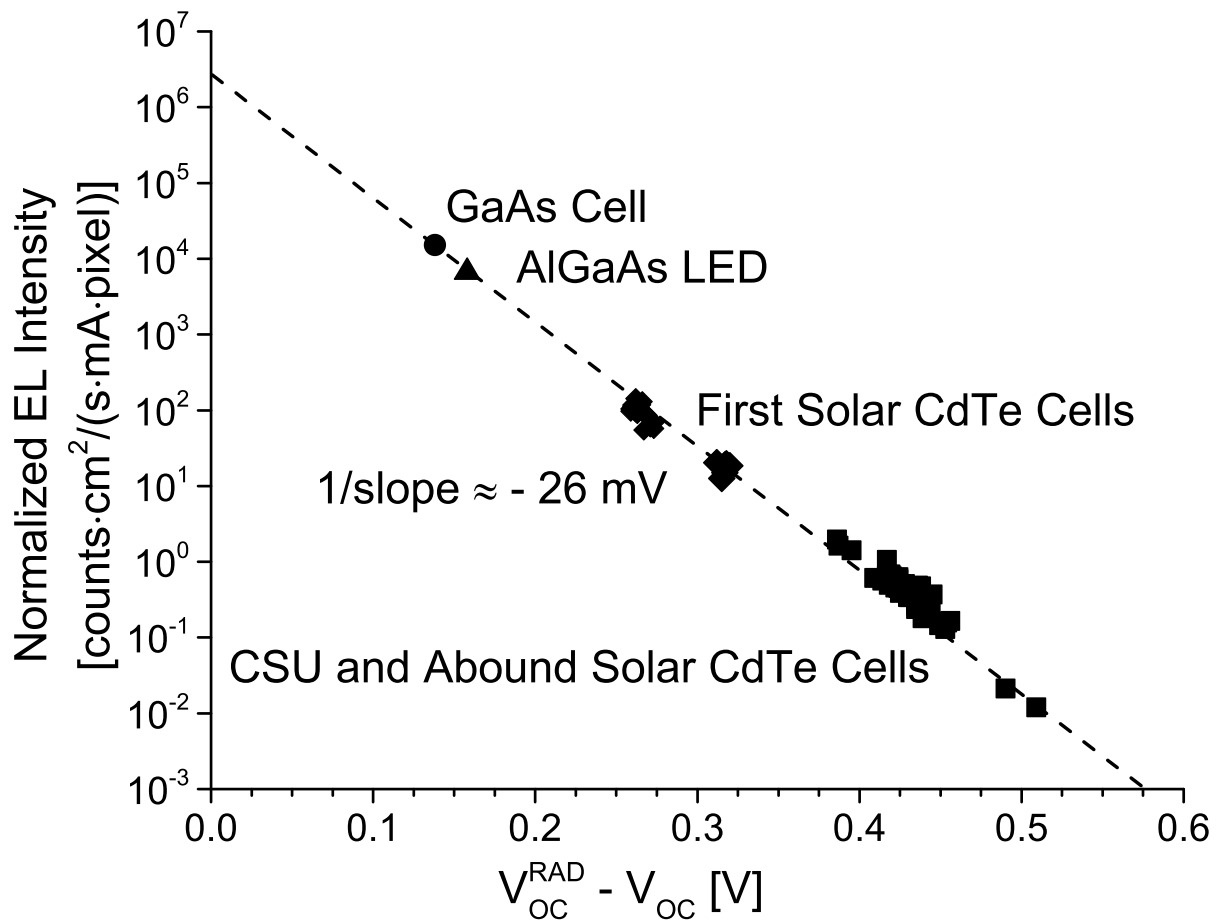


Figure 3.2: Normalized EL intensity vs voltage deficit. Fit above has an inverse slope of approximately -26 mV, in agreement with Eq. 3.10

trend to span 8 decades of efficiency from devices made with one of seven different band gaps.

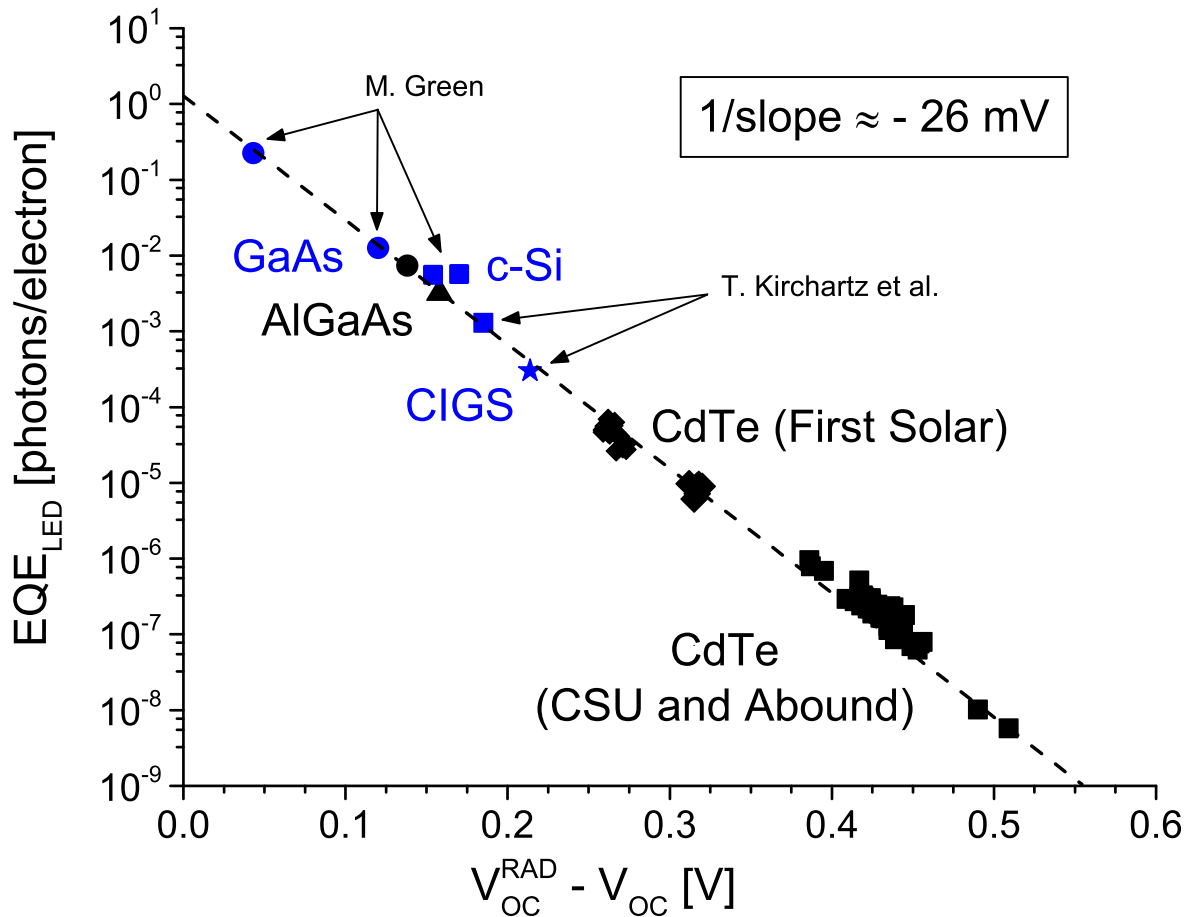


Figure 3.3: EQE_{LED} vs voltage deficit, black data points are from Fig. 3.2 and are overlaid with two sets of calibrated cells published elsewhere [12, 13]. Intercept of fit is very near unity with inverse slope approximately equal to -26 mV, in agreement with theory.

3.4 EL Uniformity

Fig. 3.4 is the EL image of three circular CdTe cells and a GaAs cell with their respective open-circuit voltages listed. All CdTe cells share the same color scale, keyed to the exponents in Fig. 3.2. In Fig. 3.4, cell (a) is the typical CSU CdTe cell (discussed in Sect. 1.4) with uniform EL intensity, cell (b) is a CdTe cell with a less-uniform window layer but higher

voltage, cell (c) is a CdTe cell with non-uniform temperature profile during its chlorine passivation treatment, and cell (d) a GaAs reference cell.

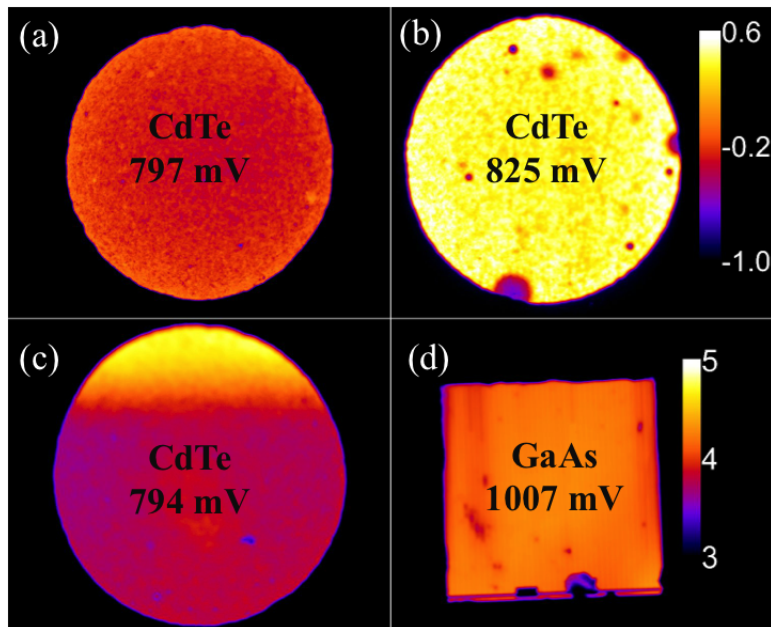


Figure 3.4: EL images of three circular CdTe cells and a GaAs cell with various degrees of non-uniformity and devices respective open-circuit voltage listed. All CdTe images have the same color scale; GaAs has a separate scale.

Histograms of three of the cells from Fig. 3.4 are plotted in Fig. 3.5 with each curve's peak normalized to unity. Cell (a) has a relatively uniform EL emission (15%), where the higher-voltage CdTe cell, cell (b), has a slightly wider EL distribution (18%) and a tail at lower intensities, as reflected in its EL image in Fig. 3.4. Cell (c) has two distinct EL intensities, and a voltage similar to cell (a) with a narrow EL distribution (12%) with a tail at higher intensities (not shown in Fig. 3.5). Cell (d) also displays some non-uniformity (20%) because some of the front-contact bus bars have a physical break in them. Despite non-uniformities, the samples all fall on the dashed line in Fig. 3.2.

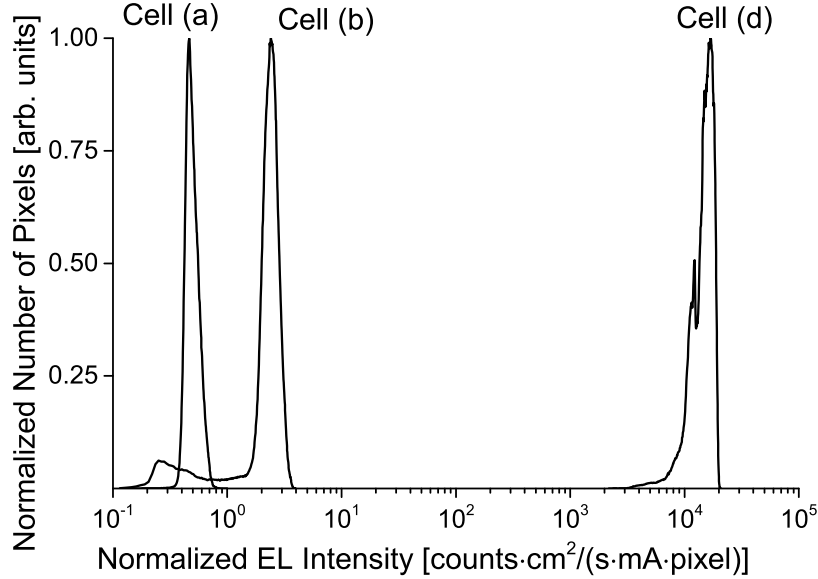


Figure 3.5: Histogram of two CdTe cells and a GaAs cell, normalized to their maximum value. Cells' EL images can be seen in Fig. 3.4.

3.5 Breakdown of the Reciprocity Relationship

EL is inherently a measurement performed in the dark, since if there were any illumination then photoluminescence (PL) superimposed on the EL signal would also be observed. Consequently, EL only contains information on the dark J-V curve and thus, asking it to predict a value dependent on the light-generated J-V curve is only possible if superposition of the light and shifted dark J-V curves holds. One reason why superposition of the dark J-V curve may fail is due to barriers in the device in which case, Eq. 3.10 would not be expected to hold, as shown by Wang *et al.* [25] and discussed by others [12].

As an example, a cell made with a barrier in the window layer by the oxygenation of CdS, as discussed in [22], was investigated. Major non-superposition of the light-dark J-V curve can be seen in Fig. 3.6(a), likely due to barrier formation in window layer, and consequentially, this cell does not follow the dashed line in the earlier figure, see Fig. 3.6(b). Based on the measured EL intensity and the trend, as shown in Fig. 3.2, the expected voltage of this cell would be 0.82 V ($V_{OC}^{RAD} - V_{OC} = 0.39$ V), significantly different from its measured open-circuit voltage of 0.46 V. This difference could be anticipated, since superposition of

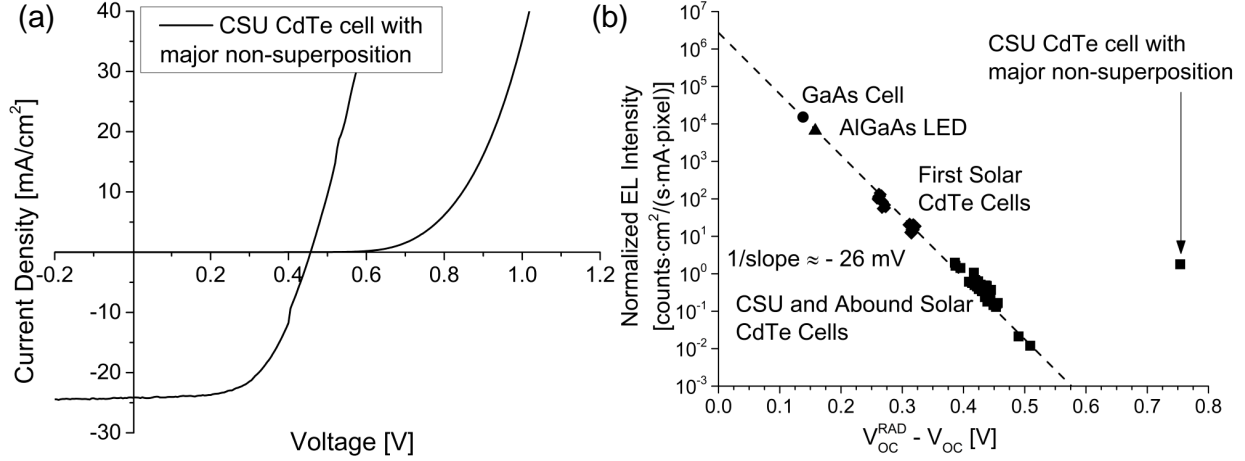


Figure 3.6: (a) J-V curve of cell with major non-superposition. (b) Large deviation from the fit for well-behaved cells.

the J-V curve fails badly, violating one of the assumptions in the derivation of Eq. 3.10. The open-circuit voltage predicted by EL is in fact similar to that which a translation of the dark J-V would also predict.

3.6 Temperature Dependent EL

Temperature dependent EL and J-V measurements were performed on CdTe cells. The minimum temperature was limited due to condensation buildup on the glass, while maximum temperature used is limited due to concern about potential device instabilities [26], so the temperature range was limited.

Fig. 3.7(a) is a plot of two cells' normalized EL intensity as a function of voltage deficit with cell temperature of 313 K, 298 K, and 283 K. Fig. 3.7(b) and (c) are J-V-T graphs of the cells used in (a). The temperature dependence of the cells' open-circuit voltage is well-behaved and no obvious lack of superposition can be seen in J-V curve, one of the assumptions in derivation of Eq. 3.10.

The three lines drawn in Fig. 3.7(a) are fits to log of data where the slope was fixed at measured value and the intercepts were allowed to vary, results are listed in Table 3.2. The

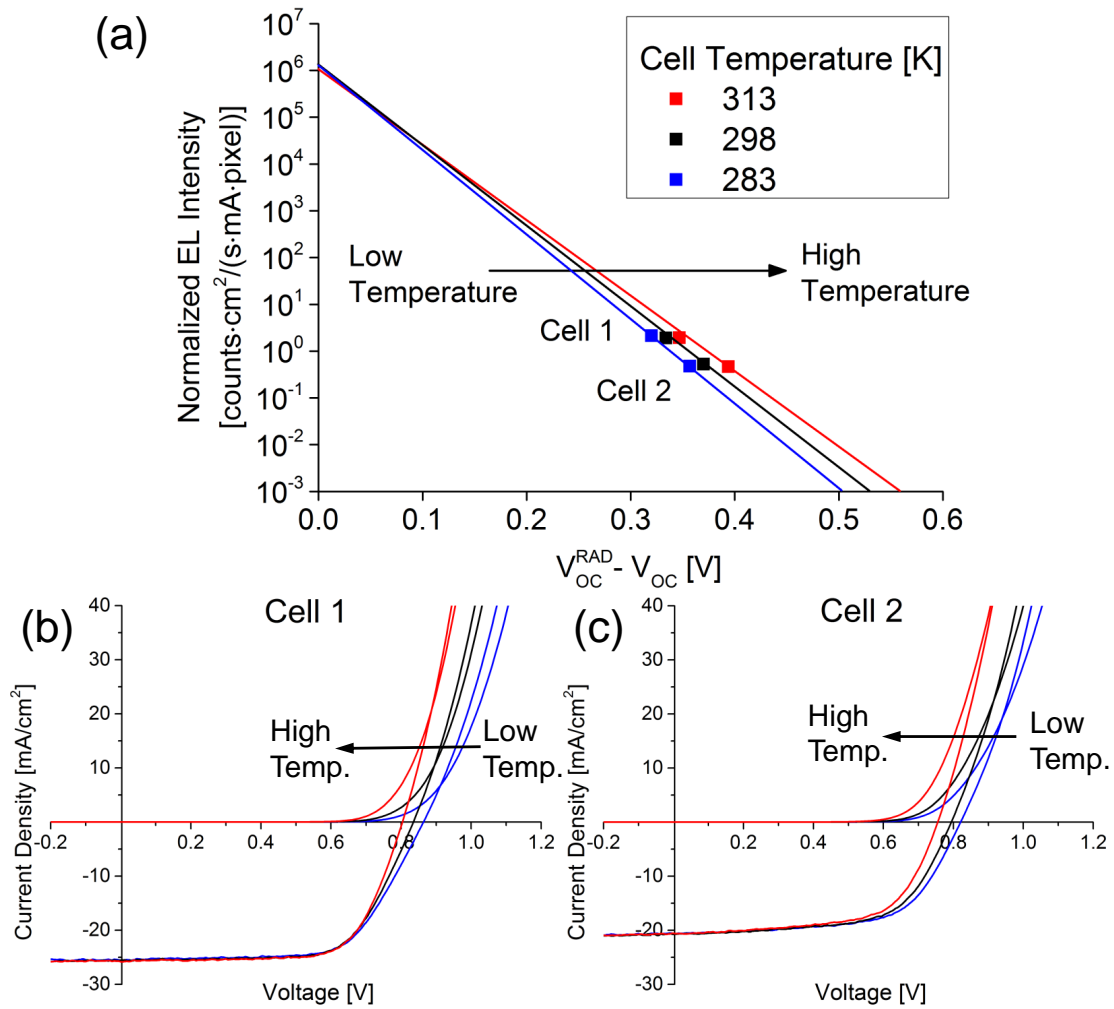


Figure 3.7: (a) Normalized EL intensity as a function of voltage deficit for three temperatures, results are in agreement with Eq. 3.10. (b) and (c) are J-V-T graphs of cells from the data plotted in (a).

intercept of the three lines are in agreement with each other as well as the line drawn in Fig. 3.2, although the temperature range is too small to draw firm conclusions.

Table 3.2: Table of parameters for fit of data in Fig. 3.7(a). Slope was fixed to known temperature and intercept was allowed to vary.

Temp. [K]	1/slope [mV]	Intercept [counts·cm ² /(s·mA·pixel)]
313	27.0	10 ^{6.0±0.1}
298	25.7	10 ^{6.1±0.2}
283	24.4	10 ^{6.2±0.2}

The cells in Table 3.2 are in good agreement with Eq. 3.10 for temperatures measured. Five cells were initially measured. However, only two of the cells follow trend as superposition of the light and dark J-V curves for the others failed at the reduced temperatures, one of the main assumptions in the derivation of Eq. 3.10 and discussed by others [12, 25].

3.7 Summary of EL Intensity-Voltage Deficit Relationship

EL from solar cells has been found to confirm the reciprocity relation over a very broad range (six decades of intensity). The normalized EL intensity correlates very well with the difference between ideal and measured open-circuit voltage from devices that include a GaAs cell, an AlGaAs LED, and several CdTe cells with large variations in manufacturing. The magnitude of the inverse slope was approximately -26 mV, in agreement with theory [20], despite non-uniform EL emission in several cases. Data points were overlaid with cells of calibrated EQE_{LED} [13, 12]. Intercept from the fit is found to be very near unity, in spite of using devices with one of seven different band gaps. The results also suggest that the reciprocity relationship does not hold for devices with measured cell open-circuit voltage not equal to the voltage across the primary cell diode, as is the case for a cell with major non-superposition.

Chapter 4

INHOMOGENEITIES IN SMALL-AREA CELLS

EL is a powerful technique for identifying inhomogeneities in cells of small-area (approximately 1 cm²) as well as modules (typically on the order of 1 m²), since EL is significantly more sensitive to defects than are other common electronic characterization techniques such as J-V or QE. Selected defects from CdTe cells are described in this chapter along with their corresponding signatures in EL images, NIR images (from the same location), J-V, and either QE or LBIC. Of the possible QE measurements (spectral, LBIC, with and without a voltage bias), only those which can provide information on the defect are tabulated. LBIC maps presented were generated with an illumination wavelength of 638 nm. A summary of the findings can be found in Table 4.1 with discussion of each defect type in the sections that follow. It is important to note that when using EL, or any other spatial mapping system to identify defects, it is critical to have a good understanding of the manufacturing process of the devices under test, since each process is prone to different defect types.

Cells are straight forward to study as they generally do not have a significant lateral voltage drop across the TCO, nor are they connected in series with other cells. A cell can be considered as three different layers: a back-contact, the primary diode with the appropriate parallel shunt resistance, and the TCO layer [19]. No defects with the TCO film have been observed with EL as this layer is usually robust as supplied by the glass manufacturer.

Although EL is very sensitive to defects, it alone can only provide information about the quality of the diode junction and associated electrical contacts (back-contact, TCO, interconnects, etc..). A simplistic view of how best to interpret EL images is listed as the expression below,

$$\text{EL Intensity}(x, y) \propto J(x, y) \cdot t_{\text{exposure}} \cdot EQE_{LED}(x, y), \quad (4.1)$$

Table 4.1: List of defects with various techniques used to identify them. The ability for a measurement technique to identify defect is indicated with either a checkmark (\checkmark) meaning likely, a circle (\circ) meaning plausible, an x (\times) meaning unlikely. Of the possible QE measurements, only those which can identify the defect are listed.

Identified Defect in Cell				
Defect Type	J-V/QE	EL Image	NIRR Image	LBIC Map
Weak-diode areas	\times/\times	\checkmark	\circ	$\lambda = 405 \text{ nm}, 638 \text{ nm}$
Cell delineation in delete region	\checkmark/\circ	\checkmark	\times	$\lambda = 405 \text{ nm}, 638 \text{ nm}$
Non-uniform Cl passivation	\circ/\times	\checkmark	\times	$\lambda = 638 \text{ nm}$
Holes in back-contact	\times/\times	\checkmark	\checkmark	$\lambda = 638 \text{ nm}$
High-resistance foreign layer	\checkmark/\times	\checkmark	\checkmark	$\lambda = 405 \text{ nm}, 638 \text{ nm}$
High back-contact sheet resistance	\circ/\times	\checkmark	\times	\times

where, $J(x, y) \cdot t_{exposure}$ is the locally injected carrier density and $EQE_{LED}(x, y)$ (External Quantum Efficiency of an LED) is the local probability of injected carriers to recombine radiatively. For well-behaved small-area cells, $J(x, y)$ is very uniform over cell area as $J(x, y)$ is dependent on the back and front-contact sheet resistance uniformity and magnitude. Although there exists higher-order corrections to interpreting EL images [18], these corrections are typically much smaller than the spatial variations in $EQE_{LED}(x, y)$ or $J(x, y)$, which can be on the order of one or many decades.

Although EL images are proficient at illustrating the location and severity of defects with potentially high spatial resolution ($\sim 4 \mu\text{m}/\text{pixel}$) and relatively short measurement times (100 seconds/image), their ability to identify the cause of such defect is limited. EL used in concert with LBIC, however, makes for a powerful ensemble as LBIC can probe different film layers at arbitrary voltage bias conditions, albeit with increased measurement times ($\sim 40 \text{ min.}/1 \text{ cm}^2$ scan area). At the CSU Photovoltaics Laboratory, EL has been employed as technique for screening of cells and of those cells measured, a select few with defects of interest are characterized with LBIC.

4.1 Typical CSU CdTe Cell

A typical CSU CdTe cell is presented as a baseline for the following sections. Analysis of J-V curve and further in-depth whole-cell electrical characterization measurements of cell can be found in Sect. 1.4. Fig. 4.1 is the normalized EL image (a), NIR image (with inverted LUT) (b), LBIC map at 0 V (c) and 0.6 V forward bias (d) and J-V curve (e) of the typical CSU CdTe cell.

False coloring is applied to all EL images however the color scale may be varied from sample to sample, since the EL intensities can vary by many decades between samples [23]. EL intensity listed is on a \log_{10} scale and are in units of $[\text{counts}\cdot\text{cm}^2/(\text{s}\cdot\text{mA}\cdot\text{pixel})]$, keyed to the graph in Fig. 3.2. EL images of CSU CdTe cells can have an overall mottled appearance due to a slightly non-uniform electrical resistance of the carbon/acrylic back-contact layer

used. When EL images of CSU cells are collected, attention is given to the orientation of the cell in reference to the cell's position on its substrate.

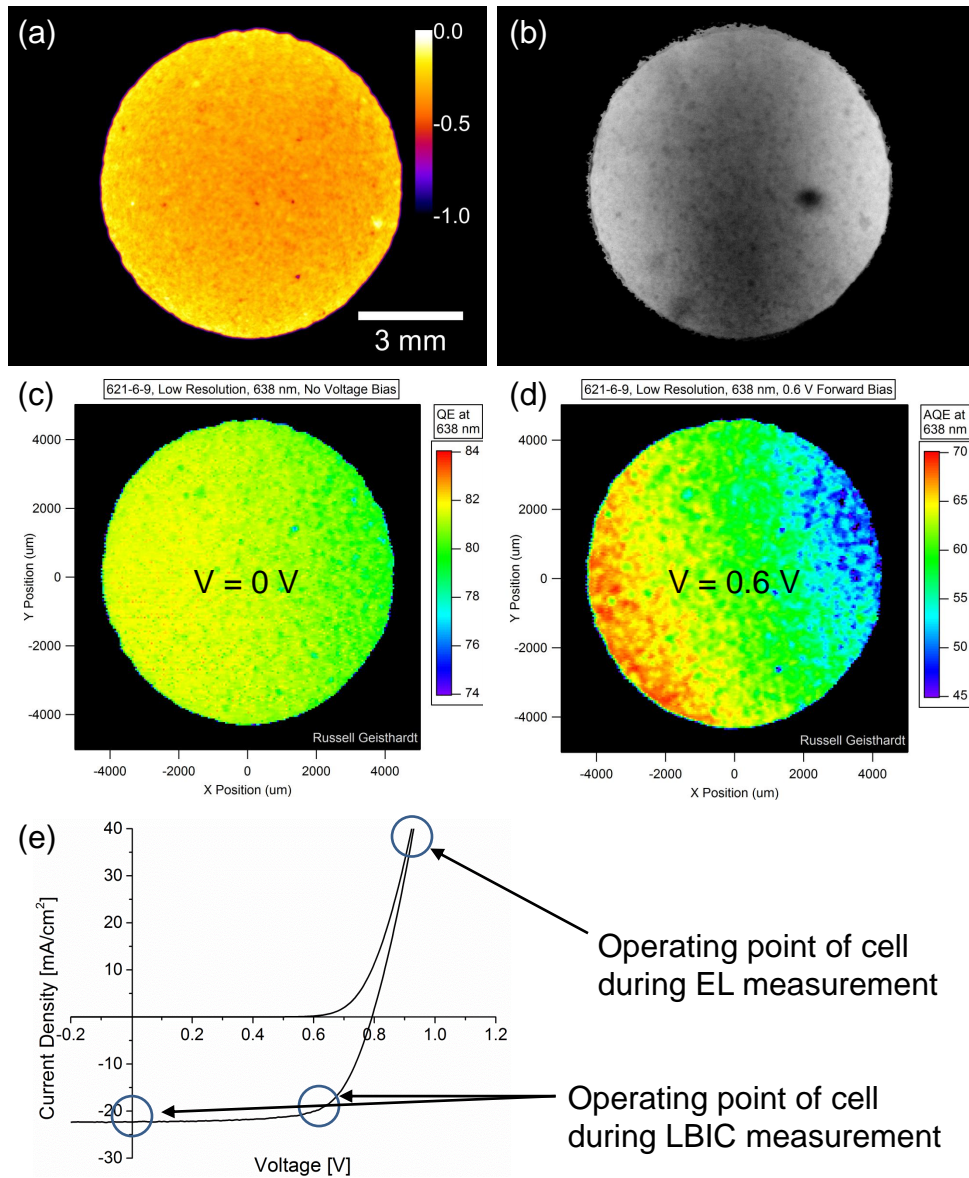


Figure 4.1: Typical CSU CdTe cell with its normalized EL image (a), Near-Infrared Reflection (NIRR) image with inverted LUT (b) LBIC map at 0 V bias (c), LBIC map at 0.6 V bias (d) and J-V curve (e) illustrating the operating point of cell during EL and LBIC measurements.

The NIRR image of a cell is in the same location as its EL image since images are collected sequentially without movement of equipment. NIRR images are presented with a Gray (black and white) Look-Up Table (LUT) and the intensity and contrast are not

preserved from one NIR image to the next, since its function is to highlight defects and color scaling is subjective. NIR brightness over cell area is not uniform (over a 5 mm length scale) due to non-uniform illumination of the sample whereas small variations in intensity can be seen on a sub-mm length scale and is typically attributed to slight variations in the local material composition of the carbon/acrylic layer. The edge of cell in NIR image appears rough as cells are manually delineated with a sandblaster, and incomplete delineation can occur at the cell edge, i.e., the conductive back-contact delineates more readily than the CdTe film. Consequently, edge roughness does not appear in device's EL image to same degree as NIR image.

Fig. 4.1(c) is of a LBIC map of cell operating at 0 V forward bias and is considered to be reasonably uniform in response. Region of cell with a reduced response is exacerbated at 0.6 V forward voltage bias relative to remaining region, see Fig. 4.1(d). This behavior is typical in most CdTe cells.

Devices J-V curve illustrates the operating point of a cell while its EL image is being collected, 40 mA/cm².

4.2 Weak-Diode Areas

A weak-diode is modeled as a diode with an increase in saturation current density, J_0 , in Eq. 1.3, resulting in a premature turn-on voltage. Weak-diode areas are expected to exhibit a significantly reduced EQE_{LED} since their J-V curves would predict a reduced open-circuit voltage, as described by Eq. 3.1. In this section, cells with weak-diode areas as a result of residuals on the glass prior to film deposition is discussed. Although the cells presented in this section have been chosen as an example of such a defect, other cells discussed in this chapter exhibit similar behavior albeit from different causes.

One of the first processes in the manufacturing of cells is proper cleaning of the glass substrate prior to film deposition. Commercially available glass with a TCO material deposited on it can be purchased in large sheets which are often cut into smaller substrates

for cell deposition. This process may introduce cutting oil, roller marks, organics from improper operator handling or other contaminants on the glass which need to be thoroughly cleaned and at times can be stubborn in spite of a thorough glass-wash process, or in the case presented, residual water marks from the glass-washing process may persist.

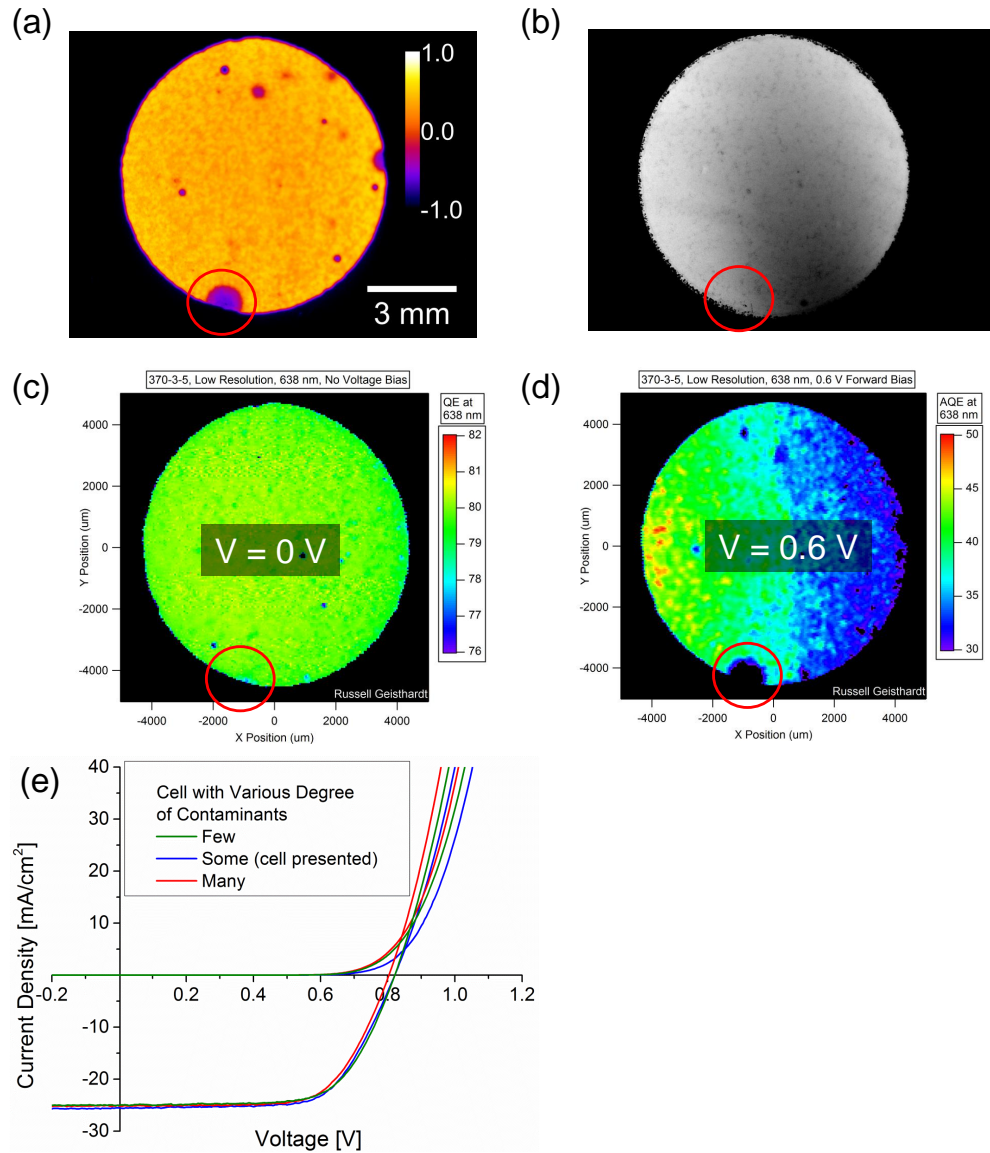


Figure 4.2: Cell with a weak-diode area (highlighted) with its normalized EL image (a), NIRR image (b), LBIC map at 0 V bias (c), LBIC map at 0.6 V bias (d), J-V curves of cells with various degrees of contaminants (e).

Of the different ways a contaminant may manifest itself in EL, one of the more obvious and typical is a circular dark spot, typically on the order of 0.1 mm - 2 mm in diameter. Fig. 4.2 is of a typical CdTe cell employing a sputtered oxygenated CdS window layer with its normalized EL image (a), NIR image (b), LBIC map at 0 V bias (c), LBIC map at 0.6 V bias (d) and J-V curves of cells with various level of contamination (e).

The circular dark spot highlighted in Fig. 4.2(a)-(d) is a strong indicator of a residual on glass prior to film deposition, which is not reflected in cell's NIR image, Fig. 4.2(b). Unlike LBIC map measured at 0.6 V (d) and EL image (a), highlighted defect does not present itself in LBIC map measured at 0 V (c). This suggests the highlighted defect has a large saturation current density (reduced EQE_{LED}) which turns-on prior to the remaining well-behaved regions of the cell and is characteristic of a weak diode, as demonstrated by Fig. 4.2(d).

The J-V curve of cell under test is contrasted with other oxygenated CdS samples from the same substrate, with different degrees of contamination (see Fig. 4.3(a) for devices' normalized EL images). Little difference can be seen between the J-V curves of the oxygenated CdS cells of different contamination levels in spite of almost a decade difference in defect area, suggesting that this defect type is fairly benign in effecting device efficiency.

Normalized EL images of devices with various degrees of contamination on a \log_{10} scale are presented in Fig. 4.3(a) with their histogram on a linear scale in 4.3(b). The fractional area occupied by the dark spots were calculated from Fig. 4.3(b) and is found to be approximately 12% for device with many contaminants, 4% for device with some contaminants and 2% for device with few contaminants.

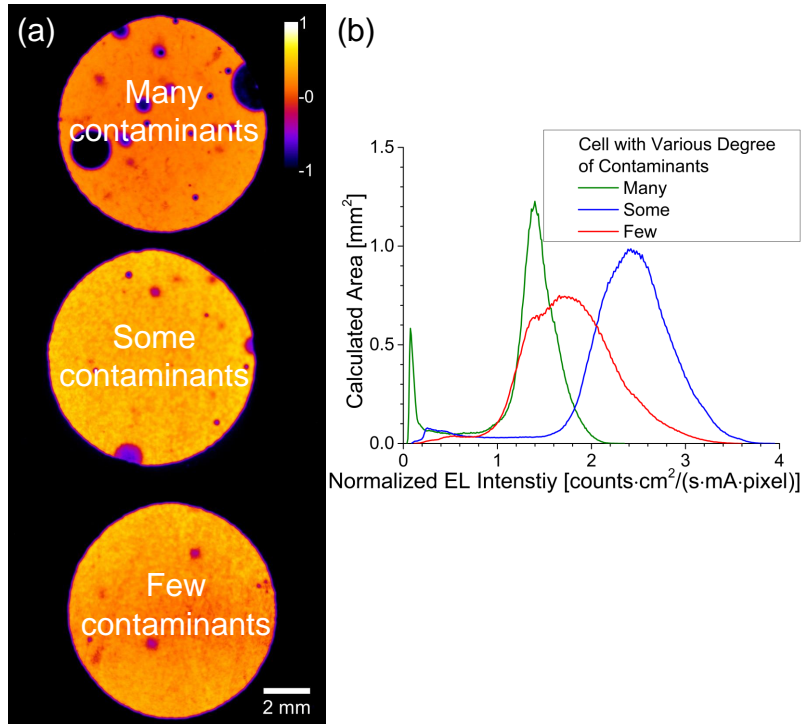


Figure 4.3: (a) Normalized EL images of cells with various degrees of contaminants with \log_{10} scale and their corresponding EL histograms (b) with linear scale.

4.3 Cell Delineation in Delete Region

Of the various defects which can occur with a CSS-deposition technique, delineation of a cell too close to substrate edge can be one of the more detrimental defects affecting cell performance. This region of the substrate (referred as the 'delete region') is known to operate at an elevated temperature during film deposition [27], which can lead to various problems, the most obvious of which is a thin CdS film [28].

In this section, a cell partially delineated in the delete region is discussed. The CdS film thickness for a typical CSU CdTe cell is 120 nm, measured at the center of the substrate and is relatively uniform over relevant area of substrate [28]. The cell's open-circuit voltage will be reduced significantly if the CdS film thickness were to fall below a threshold value and will continue to do so with decreasing film thickness [8].

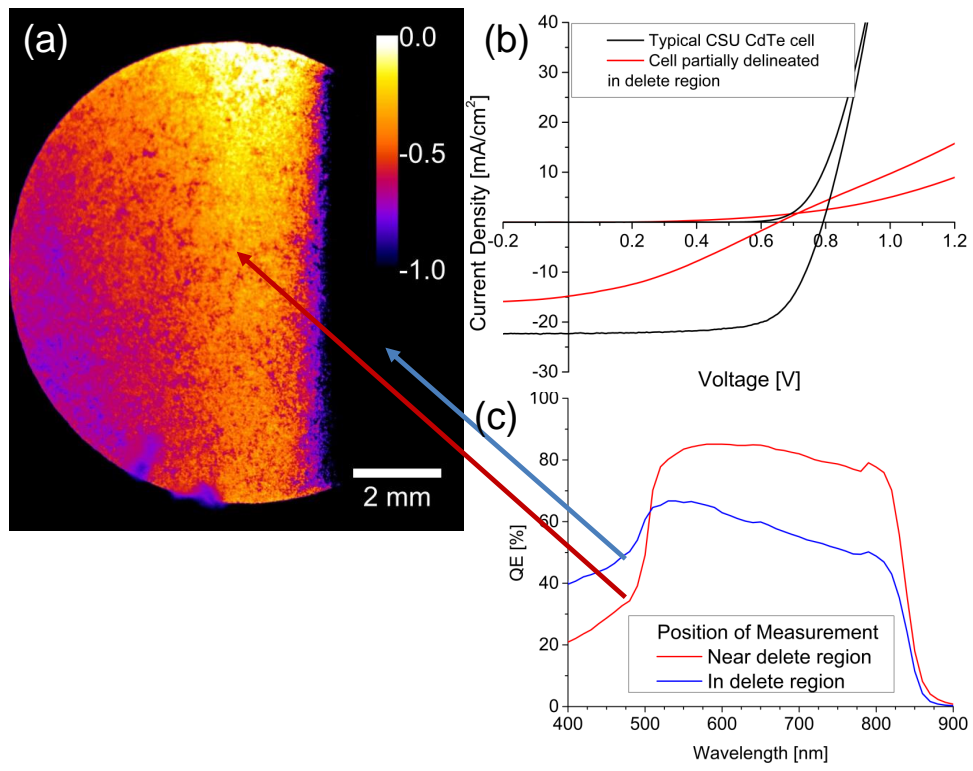


Figure 4.4: EL image of cell partially delineated in delete region of substrate, resulting in a thin CdS film thickness at edge of cell. Cell's normalized EL Image (a), J-V curve (b) and QE curves comparing the two regions (c).

Fig. 4.4 is of a cell partially delineated in the delete region with its corresponding EL image (a), J-V curve (b), and QE of the two regions of interest (in and near delete region) (c). Devices EL image, Fig. 4.4(a), demonstrates two regions of the cell (of high and low EL intensity) with a well-defined border which follows substrate geometry, corresponding to the cell delineated near the delete region (luminescent part of cell) and in the delete region (non-luminescent part of cell).

The J-V curve of device under test is contrasted with the typical CSU CdTe cell in Fig. 4.4(b). A reduction in short-circuit current density can be observed along with a decrease in fill-factor and a high series resistance, indicating additional material problems with the device. QE of the cell, Fig. 4.4(c) collected at two regions of the cell are compared and show a decrease in CdS film thickness due to increase response for wavelengths of energy greater than the CdS band gap of 2.47 eV (502 nm). The QE measurements indicate LBIC would also identify this type of defect: reduced signal at 638 nm, enhanced at 405 nm.

4.4 Non-Uniform Chlorine Passivation

As described elsewhere [6, 7, 8, 9], Cl passivation of polycrystalline CdTe cells is a critical part of the manufacturing process as device performance is highly dependent on passivation quality. As with most CSS processes, temperature uniformity of substrate is key for uniform device performance and in the presented case, material passivation. In addition to variations in material passivation, significant variations in other fabrications steps near the substrate edge is also possible, such as the case presented in the previous section.

In this section, the effect of non-uniform substrate temperature during the Cl passivation process is discussed. During the CdTe passivation process at CSU, one end of the substrate is actively heated, whereas the other end of the substrate is passively cooled, resulting in an unintentional lateral temperature gradient [27]. Consequently, a build-up of CdCl₂ salt can occur on the cooler end of the substrate.

Fig. 4.5(a) is a montage of EL images of cells from the same substrate, oriented and located the same as they were on substrate with their open-circuit voltage listed. Fig. 4.5(b)

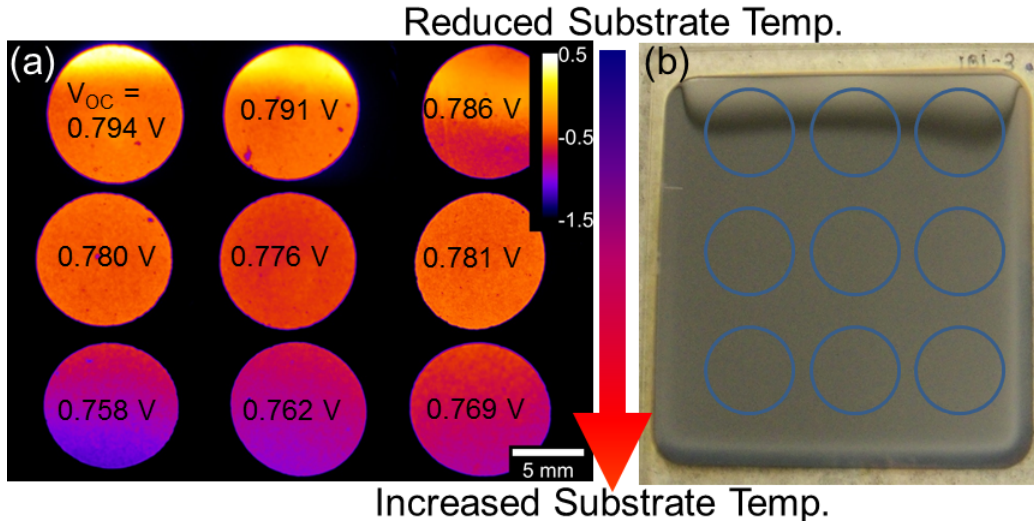


Figure 4.5: EL image of cells (a) and optical image of the substrate (b) with a non-uniform chlorine passivation treatment as a result of lateral temperature gradient on substrate. EL images have cells' respective open-circuit voltage listed. Circles drawn on optical image indicate position of cells on substrate.

is an optical image of the same substrate immediately following its Cl passivation process, note the CdCl_2 salt build-up (white in color) on the end of substrate labeled with a reduced substrate temperature. Circles drawn on optical image represent the location of the 9 delineated cells.

Variations in EL intensity in Fig. 4.5(a) over substrate can be as large as two decades, due to variations in the local EQE_{LED} . EL is of course sensitive to much smaller variations and can be used to monitor the V_{OC} variation.

4.5 Holes in Back Contact

Holes may exist in the back contact of a cell. This can occur for a number of reasons such as: incomplete film deposition (as in the case presented) or due to improper handling of a cell with a delicate back-contact. This defect can manifest itself in several ways: either a dark spot in the location of the absent back contact or, in the highlighted case presented, a bright spot due to an electrical short through the more-resistive carbon/acrylic layer.

As described in Section 1.3, CdTe cells manufactured at CSU have a two-part back contact: a carbon/acrylic paint and a nickel/acrylic paint (improve lateral conductivity). The paint to be applied needs to be prepared in advance and is then applied manually via a spray gun, with the nickel/acrylic paint applied after the previous coat of carbon/acrylic has sufficiently cured. This highly manual process is prone to human error and as a result, small holes in the carbon/acrylic layer have occasionally been observed as a result of improper application of the carbon/acrylic layer. Fig. 4.6 is a schematic of the CdTe stack structure with and without holes present in the carbon/acrylic back-contact layer.

A cell with holes in the graphite/acrylic paint layer can be seen in Fig. 4.7 with its corresponding EL image (a), NIRR image (b), optical transmission image (c) and LBIC map performed at 0 V bias (d). The EL image of cell demonstrates small bright and dark spots with one selected defect highlighted with a red circle. It is suspected that the bright spots are locations where the nickel/acrylic layer is in direct contact with the semiconductor free surface, bypassing the more resistive carbon/acrylic layer, as depicted in Fig. 4.6. The bright ring around cell is due to the delineation process and has been investigated elsewhere [29].

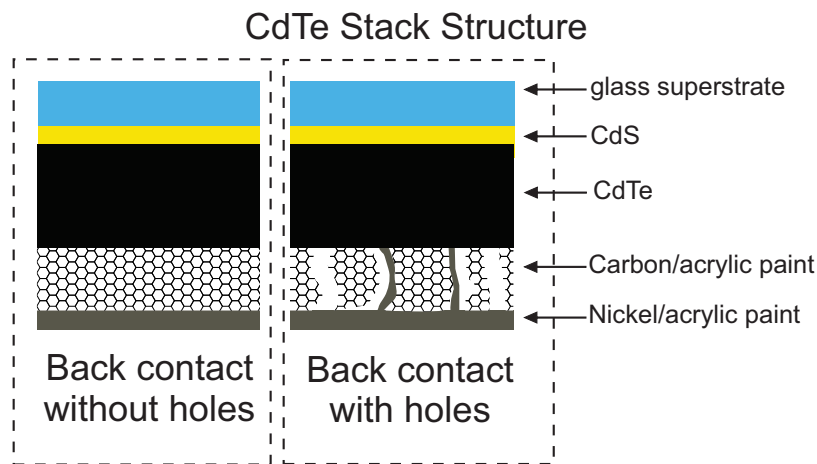


Figure 4.6: Schematic of two CdTe cells (not to scale), one without holes present (left) and one with holes (right) present in the graphite/acrylic back-contact layer.

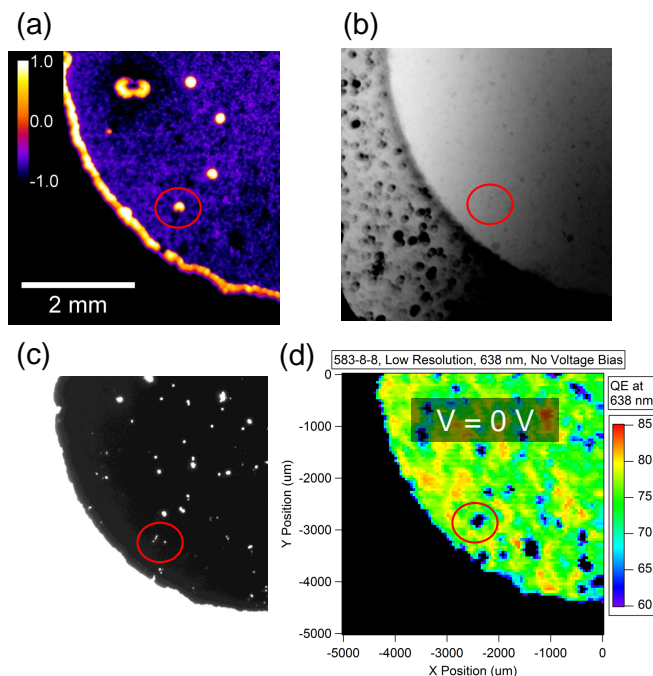


Figure 4.7: Normalized EL image (a), NIRR image (b), optical transmission image (c) and LBIC map at 0 V forward bias (d) of cell with holes present in carbon/acrylic back contact.

The NIRR image of a cell with inverted LUT can be seen in Fig. 4.7(b) with small dark spots in the same location as defects seen in EL image. Dark spots of an inverted LUT reflection image correspond to bright spots due to locations of increased light reflection. In case of highlighted defect, this would be reflection off of semiconductor/free surface, further confirmation of hole in back contact.

The optical transmission image of cell, Fig. 4.7(c), employs a 30-W halogen bulb coupled to an optical fiber (same used with NIRR images), focusing optics employ a 720-nm long-pass filter. The bright spots in this image agree with locations of defect identified in other images, demonstrating the presence of holes in the back-contact cell electrode. Fig. 4.7(d) is an LBIC image of same cell performed with no applied voltage bias and an excitation source of 638 nm. A reduced response can be seen at location of defect, further verifying the nature of the defect.

4.6 Back-Contact Sheet Resistance

A CdTe cell manufactured by First Solar was used for this section. The cell used employed a delicate back-contact which is atypical from First Solar's manufacturing process. The sheet resistance of back-contacts are determined by two parameters: material resistivity and film thickness, and hence a insufficiently thin back-contact electrode will result in a back-contact with high sheet resistance. If the back-contact sheet resistance were sufficiently large, a voltage drop will occur at the contact location. This non-uniform voltage profile can be readily noted in a cell's EL image as the current through the diode is exponentially dependent on the locally applied voltage bias, see Eq. 1.3.

Fig. 4.8 shows an example of such a defect with its normalized EL image (a), line cut profile of normalized EL image (b) and J-V curve (c). The NIR image and QE of cell is not provided as this particular defect will not present itself with these techniques. A bright spot can be seen in the EL image, corresponding to the location of the back-contact electrical probe. The blue dotted line in EL image represents location of line cut plotted in Fig. 4.7(b). The line-cut profile demonstrates that the EL signal at probe location to be approximately 2.5 times larger in magnitude than surrounding cell area.

The J-V curve of device under test can be seen in Fig. 4.7(c) and is compared to a similar cell with no apparent issues with sheet resistance of back-contact. The relative increase in back-contact sheet resistance can be noted in cell's J-V curve as a subtle increase in series resistance. The resistance across back-contact was measured with a digital multimeter and found to be approximately 15Ω for cell presented and 3Ω for the standard cell.

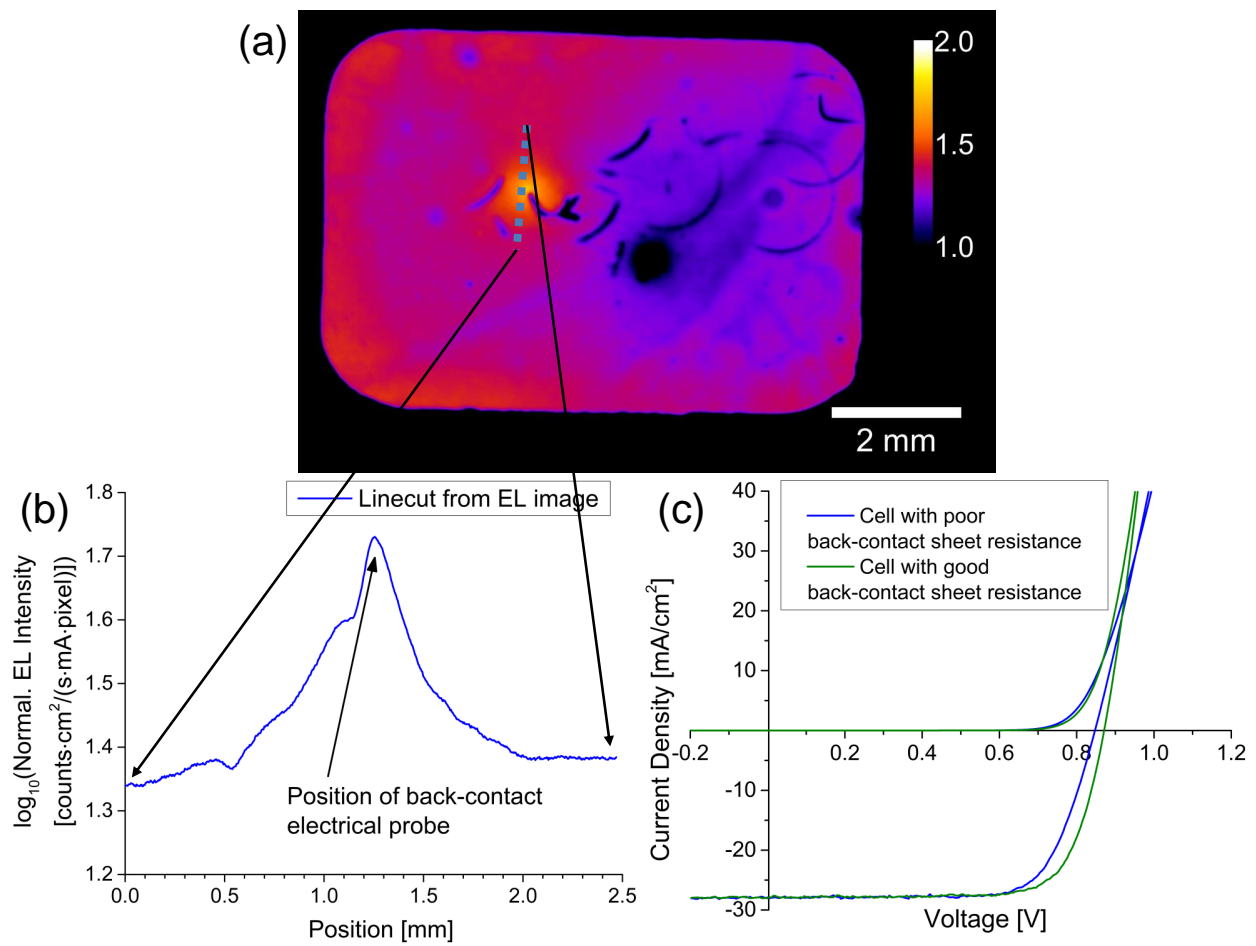


Figure 4.8: Cell with an increased back-contact sheet resistance with its corresponding normalized EL image (a), line cut from normalized EL image (b) and J-V curve of cell contrasted with cell of a reduced back-contact sheet resistance (c).

4.7 High-Resistance Foreign Layer

CdTe cells manufactured at University Loughborough's Photovoltaics Laboratory, a lab in the process of optimizing cell recipe during time of measurement, were investigated with EL. The sample shown is similar to typical CSU CdTe cell except for cell delineation, which is accomplished by depositing square gold back-contact electrodes in a regular pattern on the semiconductor free surface. The sample under test was exposed to ambient conditions for several days prior to application of the gold back-contact. It is suspected that this exposure resulted in the formation of a spatially non-uniform foreign layer of high electrical resistance on the semiconductor free surface. Fig. 4.9 is of device under test with its corresponding EL image (a), NIRr image (b) and J-V curve (c).

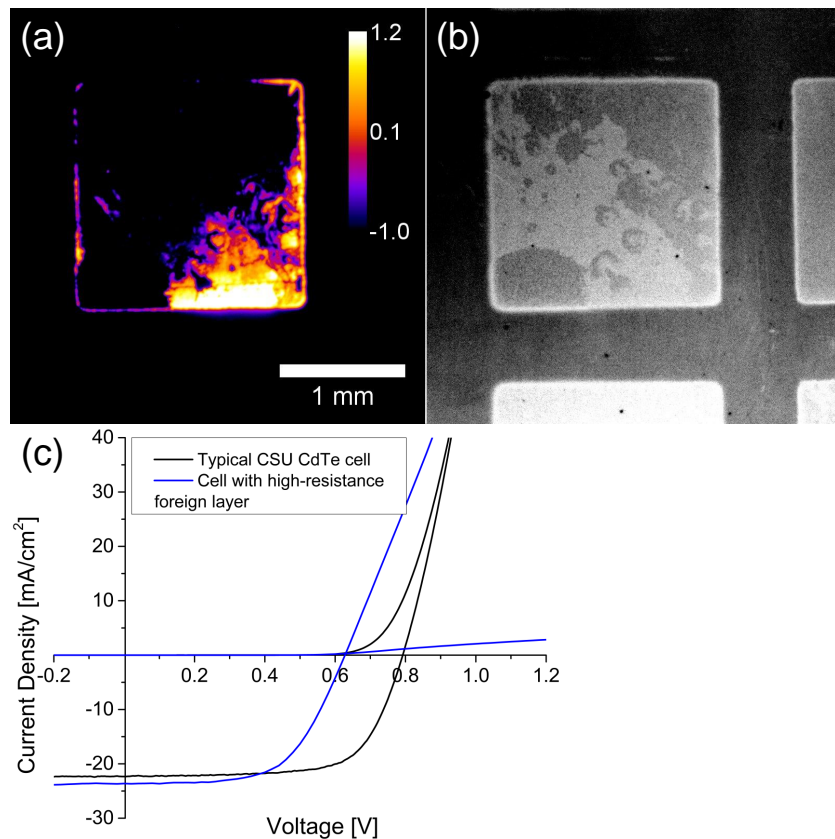


Figure 4.9: Cell with non-uniform foreign layer of increased electrical resistance between absorber and back-contact electrode with its corresponding normalized EL image (a), NIRr image (b) and J-V curve (c). Sample courtesy of Dr. Jake Bowers from University Loughborough.

A highly non-uniform EL signal can be noted in devices EL image, Fig. 4.9(a). Current crowding can be noted in image, resulting in saturation of detector (saturation point $\approx 10^1$ counts \cdot cm 2 /s \cdot mA \cdot pixel) whereas EL signal in other locations of cell are near background values.

The NIR image of cell with inverted LUT, Fig. 4.9(b), demonstrates a non-uniform reflection pattern from gold/semiconductor interface. Selected parts of pattern seen in NIR image agree with EL pattern, suggesting pattern in NIR image is partly a result of non-uniform foreign layer.

The J-V curve of device under test is compared to typical CSU CdTe cell in Fig. 4.9(c). Two cells have comparable short-circuit current densities, indicating no delamination of film as this would have resulted in a significant reduction in short-circuit current density. Furthermore, the device under test has a noticeably large series resistance in the light J-V curve, indicating the presence of a film of significantly increased electrical resistance.

Although LBIC was not measured for device under test, it is expected that this defect would have presented itself under such a measurement if it were performed with a sufficiently high applied forward voltage bias and appropriate excitation wavelength.

4.8 Summary of Inhomogeneities in Small-Area Cells

EL is a powerful technique for identifying defects in cells of small-area (~ 1 cm 2), since EL is significantly more sensitive to defects than are other common electronic characterization techniques such as J-V or QE. Selected defects from CdTe cells were described in this chapter along with their corresponding signatures in EL images, NIR images (from the same location), J-V, and either QE or LBIC. Defects identified include weak-diode areas, cell delineation near substrate edge, non-uniform chlorine passivation, holes in back contact, high-resistance foreign layer and a high back-contact sheet resistance.

Although EL images are proficient at illustrating the location and severity of defects with potentially high spatial resolution (~ 4 μ m/pixel) and relatively short measurement times (100 seconds/image), its ability to identify the cause of such defect is limited. Used in concert

with LBIC, however, makes for a powerful ensemble as LBIC can probe different film layers at arbitrary voltage bias conditions, albeit with increased measurement times (~ 40 min./ 1 cm^2 scan) and reduced spatial resolution for an entire cell (typically $\sim 100 \mu\text{m}/\text{pixel}$).

Chapter 5

DEFECTS IN MODULES

A thin-film CdTe module generally consists of an array of monolithically interconnected cells and with this added complexity comes additional defects. Furthermore, the difficulty associated with depositing films while maintaining device efficiency generally increases with deposition area. Monolithic interconnects are achieved with 3 line-scribes, typically referred to as P1, P2 and P3. Fig. 5.1 is a schematic of a cross-section of a module with the three line-scribe interconnects labeled and arrows representing direction of current flow when the module is in forward electrical bias with no illumination. Many of the defects observed in thin-film CdTe modules are shunts across a cell-delineation line scribe (intercell shunt) or a shunt through a cell (intracell shunt).

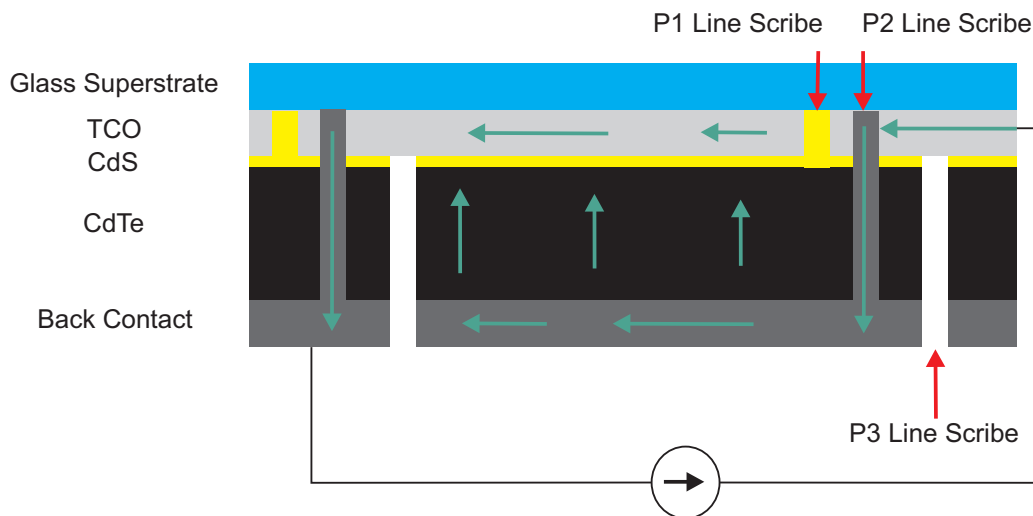


Figure 5.1: Schematic of a cross-section of a monolithically integrated CdTe module with P1, P2 and P3 line scribes (not to scale). Green arrows represent direction of current flow under forward bias and without illumination.

Both intercell and intracell shunts are considered here to be an ohmic resistor in parallel with a diode of non-linear resistance (see Fig. 1.3(b)). In the case of low-injection current

densities ($\sim 4 \text{ mA/cm}^2$), where the resistance of the diode is large compared to the resistance of the shunt, current will primarily flow through the shunt and the EL image will appear dark over an extended area. In contrast, operating the module at larger current densities ($\sim 20 \text{ mA/cm}^2$), where the resistance of the diode may be small compared to the resistance of the shunt, the EL image is only dark over a similar area near location of defect, since much of the current is flowing through the less-resistive diode. In the case presented, the affected EL area is dependent on injection current density. This defect-type may be contrasted with a weak-diode area which does not effect area surrounding defect in a significant way. This effect is typically more pronounced in the case of a intracell shunt since the film contacting the intercell shunt (metal back contact) has a much smaller sheet resistance than the film contacting the intracell shunt (TCO).

Two CdTe modules are used for discussion in this chapter, a well-behaved module and one with many defects. The modules were manufactured by Abound Solar, and they consist of CdTe cells similar to those made at CSU with the exception of an sputtered metal back-contact. The line scribes delineating the individual cells were achieved with a pulsed laser. All images presented in this chapter were collected with the macro lens and no extension tube or IR filter. EL intensities are assumed to be proportional to the product of the locally injected carriers with the probability of recombination of injected carriers to be radiative as expressed in Expr. 5.1 below,

$$\text{EL Intensity}(x, y) \propto J(x, y) \cdot t_{\text{exposure}} \cdot EQE_{LED}(x, y), \quad (5.1)$$

where, $J(x, y) \cdot t_{\text{exposure}}$ is the locally injected free carrier density and $EQE_{LED}(x, y)$ is the local probability of injected carriers to recombine radiatively. In the case of a shunt (either intra or inter), variations in EL intensity are mostly due to variations in local current density through the diode as shunts alter the local voltage bias in the conductive films contacting the shunt.

As a result of lateral current flow in the TCO and metal back-contact, a non-uniform voltage profile forms on the different layers (mostly in the TCO layer), resulting in non-uniform current flow through the diode, as illustrated in an EL image of a well-behaved module in Fig. 5.2(a) with line cut of image in (b). This is similar to the effect seen in Sec. 4.6, however, the effect is more pronounced in the typical module geometry with cell dimension on the order of 1 cm.

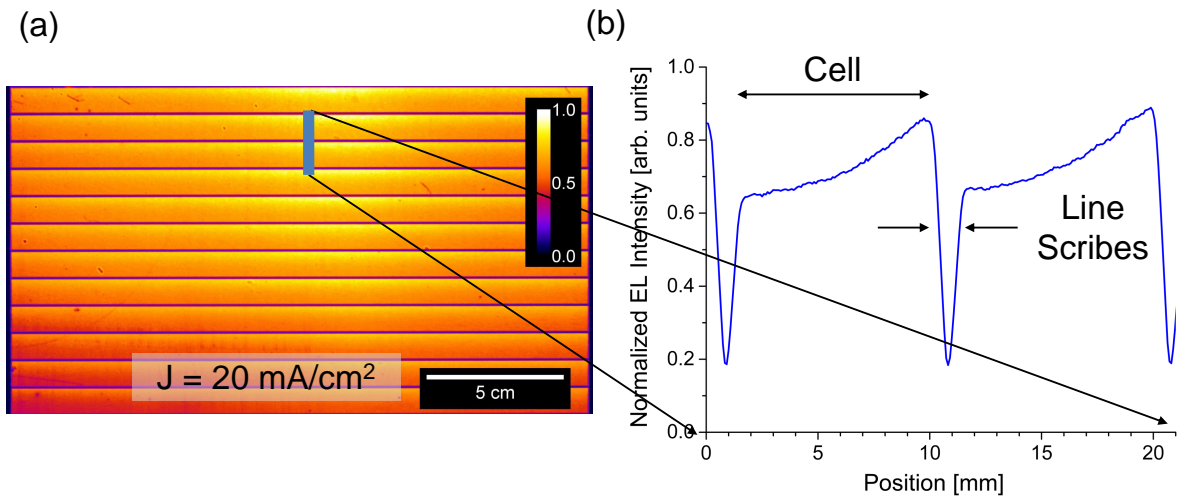


Figure 5.2: (a) EL image of well-behaved module and (b) its corresponding line cut.

In contrast to the well-behaved module, Fig. 5.3 is an EL image of a module with many defects, of which two selected defects are highlighted for discussion in this chapter: (1) is a discontinuous P3 line scribe resulting in a shunted cell (intercell shunt) and (2) is a shunt through the cell (intracell shunt). Defects discussed in this chapter are listed in Table 5.1 as well as the techniques used in identification of defects. Of the complementary techniques one may use to identify the cause and size of a defect, reflection images of the same location as their EL image counterpart are considered to be very useful as line-scribe defects tend to be a major defect-type in thin-film CdTe modules. Useful techniques for identification of defects in modules are those which provide spatial information. J-V curves of modules are generally less useful and are not presented in this chapter, since J-V curves aggregate the effect of all the defects populating a module.

Module with Many Defects

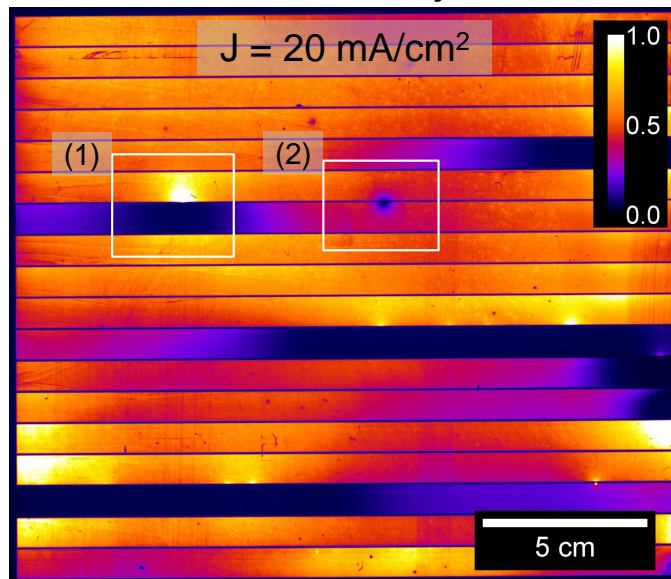


Figure 5.3: EL image of module with select defects highlighted: (1) discontinuous P3 line scribe (intercell shunt) and (2) shunt through cell (intracell shunt).

Table 5.1: List of defects with various techniques used to identify them. Ability for measurement technique to identify defect is indicated with a checkmark (✓).

Identified Defects in Module					
Defect Type		Defect Location		EL Image	Reflection Image
(see Fig. 5.3)					
Discontinuous	P3	Line	(1)	✓	✓
Scribe					
Shunt Through Cell		(2)		✓	✓

5.1 Discontinuous P3 Line Scribe

Higher optical magnification of EL image of a module with a discontinuous P3 line scribe labeled as defect (1) in Fig. 5.3 can be seen in Fig. 5.4 with an injection current density of: (a) 20 mA/cm^2 , (b) 10 mA/cm^2 and (c) 4 mA/cm^2 , and a reflection image of same location with the same scale (d) and with increased digital zoom (e). EL images are normalized to their respective injection current densities and the nominal maximum pixel response in (a). It is strongly suspected that the cause of this shunt is a result of incomplete laser evaporation of material during scribe process, since a residual feature of the intercell shunt can be seen in (e).

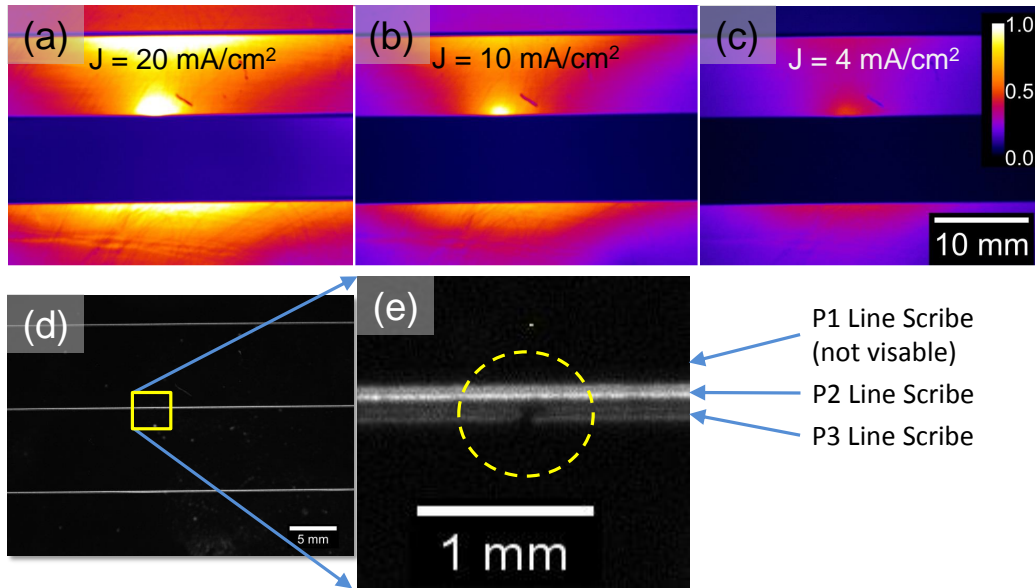


Figure 5.4: Increased optical magnification of defect (1) from Fig. 5.3 and attributed to a discontinuous P3 line scribe. EL images were collected with an injection current density of (a) 20 mA/cm^2 , (b) 10 mA/cm^2 and (c) 4 mA/cm^2 . Reflection image of defect (d) and with increased digital magnification (e).

Fig. 5.5 is a schematic of a cross-section of a module illustrating the absence of the P3 line scribe and the resulting current flow through the darkened cell. The line-scribe defect is approximately 0.13 mm in size as measured from a line cut in the optical image,

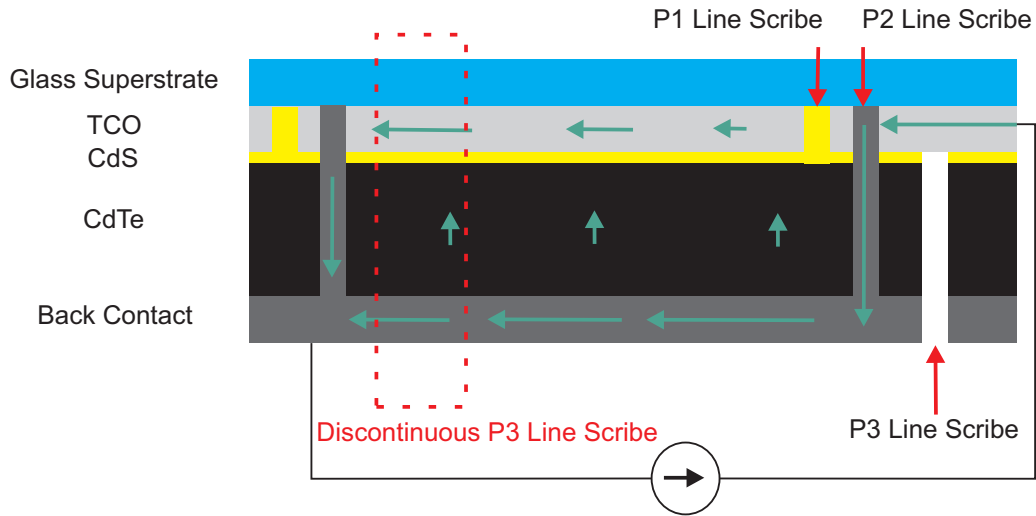


Figure 5.5: Schematic cross-section of module with discontinuous P3 line scribe (intercell shunt). Presence of intercell shunt results in a cell with much of the injection current bypassing the diode.

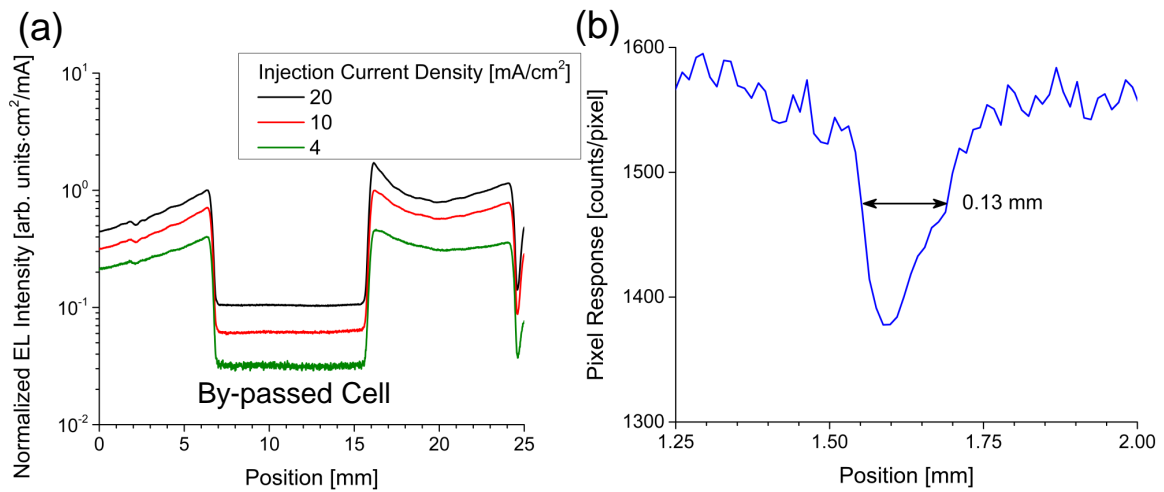


Figure 5.6: Line cut of optical image across discontinuous P3 line scribe (a). Line scribe of defect from optical image (b). Size of defect is approximately 0.13 mm.

see Fig. 5.6(b). The line cut of EL image in Fig. 5.4(a)-(c) is plotted in Fig. 5.6(a). The current through shunted cell is approximately 10% the current through adjacent cells and is nearly independent of injection current densities used, highly suggestive the resistance of the intercell shunt is much less than the diode for injection current densities used. Note in Fig. 5.3 the effected EL area resulting from defect (1) is quite large, even at high injection current densities. This is mainly due to the relatively low sheet-resistance of the electrical back-contact. This defect is sufficiently parasitic as to effect the EL intensity near the location of defect (2).

5.2 Shunt Through Cell

EL images of defect (2) in Fig. 5.3 with increased optical magnification can be seen in Fig. 5.7 with an injection current density of: (a) 20 mA/cm², (b) 10 mA/cm² and (c) 4 mA/cm². The corresponding reflection image of same optical magnification can be seen in (d) and with increased digital magnification (e).

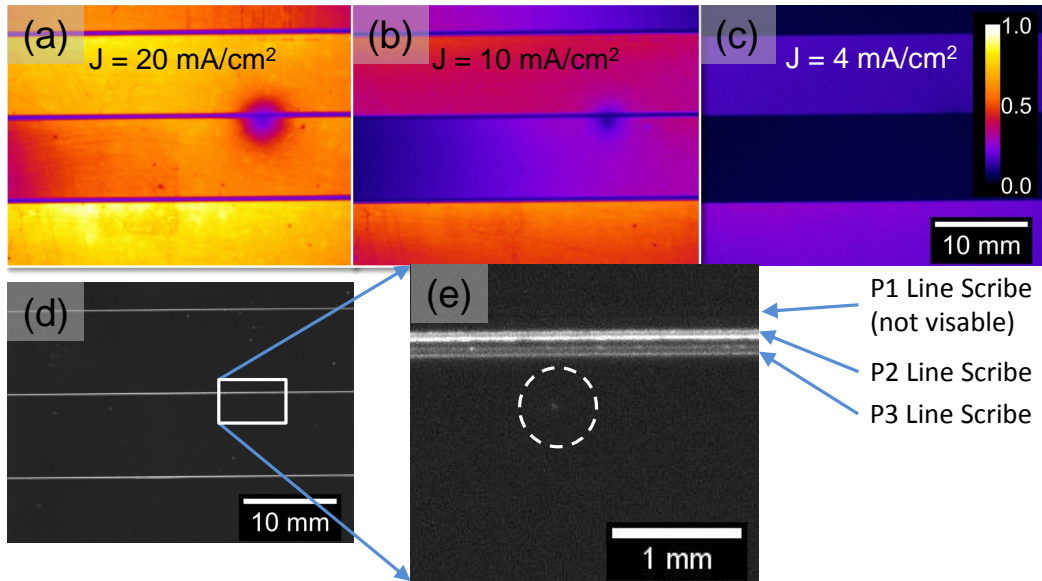


Figure 5.7: Increased optical magnification of defect (2) identified in Fig. 5.3. EL images were collected at injection current density of (a) 20 mA/cm², (b) 10 mA/cm² and (c) 4 mA/cm². Reflection image of defect can be seen in (d) and with a digital zoom in (e).

The ability to see defect in the reflection image is limited since size of defect is approximately 0.05 mm (several pixels), see Fig. 5.7(b) for line cut of defect in reflection image. Although defect is small in size, the location of defect identified in reflection image and in EL image are in excellent agreement.

It is suspected that the reduced EL signal in the shunted cell is due to the intercell shunt described in the previous section. Intracell shunt presented here effects a much smaller EL area relative to the intercell shunt since one of the films contacting the intracell shunt is of a relatively high sheet resistance (TCO).

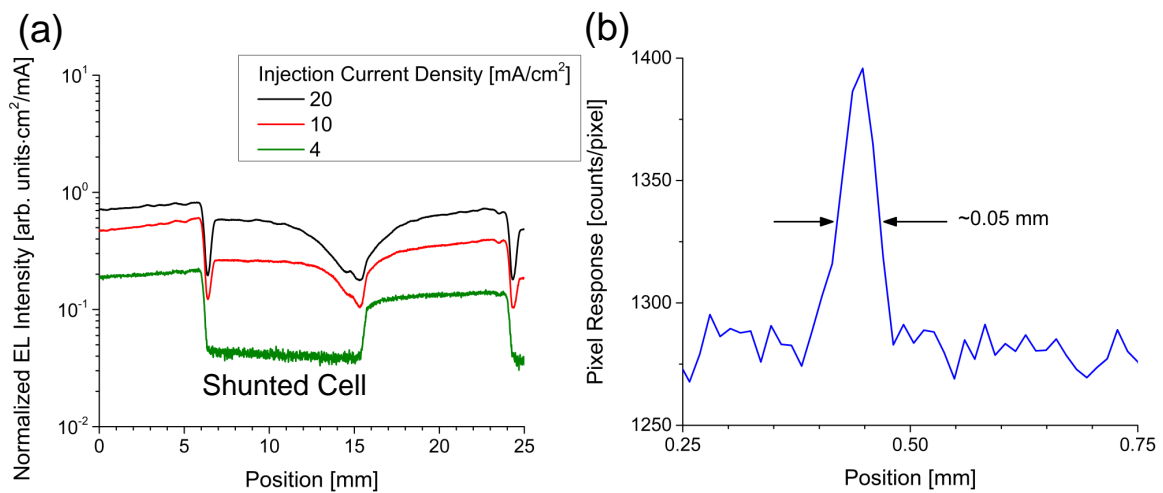


Figure 5.8: Line cut of optical image across shunt in cell. Effected area is much smaller than size of defect, approximately 0.05 mm.

Data suggests shunt is caused by metal back-contact to be in ohmic contact with the front of the cell (TCO), as illustrated by schematic of cross-section of module in Fig. 5.9.

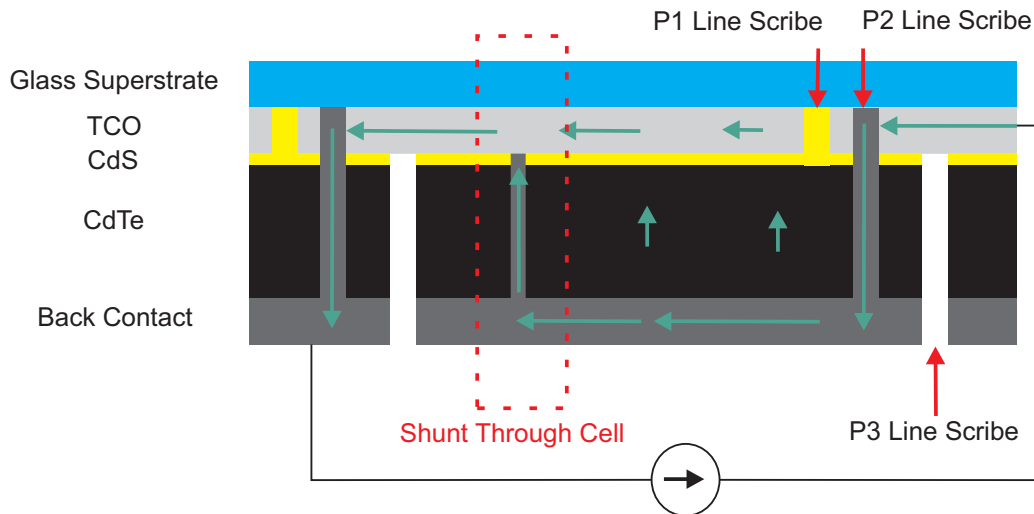


Figure 5.9: Schematic cross-section of module with shunt through cell (not to scale). Some fraction of current by-passes the more-resistive diode to flow through the less-resistive shunt.

5.3 Summary of Defects in Modules

Photovoltaic modules consist of an array of monolithically interconnected cells consisting of the P1, P2 and P3 line scribe and with the added complexity comes additional defects. In this chapter, two defects are discussed: a discontinuous P3 line scribe (intercell shunt) and a shunt through cell (intracell shunt). They are both readily identified in EL since their effected area is much greater than the size of the physical defect. In the case of the two different shunt-types presented here, the intercell shunt exhibited a much larger impact on effected EL area than the intracell shunt. This is primarily due to the relatively small sheet resistance of the back-contact contacting either end of the intercell shunt. Reflection images in the same location as EL images were found to be necessary for identification purposes. EL imaging of modules is a technique which can readily identify defects in modules, typically previously unknown to the manufacturer, with relatively short measurement time.

Chapter 6

CONCLUSIONS AND FUTURE WORK

6.1 Conclusions

Thin-film solar cells emit radiation while operating at forward electrical bias, analogous to an LED, a phenomena known as electroluminescence (EL). This process is relatively inefficient for polycrystalline CdTe devices, where even the best cells measured have radiative efficiencies below 0.01%, as most of the energy is converted into heat, but still strong enough for many valuable measurements. An EL system, built at the Colorado State University Photovoltaics Laboratory to measure EL from CdTe cells and modules, has proven to be a valuable system for identification of inhomogeneities in CdTe cells and modules.

EL intensities normalized to exposure time and injection current density were found to correlate very well with the difference between ideal and measured open-circuit voltages (voltage deficit) from devices that include a GaAs cell, an AlGaAs LED, and several CdTe cells with variations in manufacturing. Furthermore, these data points were found to be in good agreement when overlaid with calibrated EL intensity data from two additional sources. The magnitude of the inverse slope of the fit is in agreement with the thermal voltage, and the intercept at zero voltage deficit was found to have a value near unity, in agreement with theory. The expanded data set consists of devices made from one of seven different band gaps and spans eight decades of EQE_{LED} efficiencies. Temperature-dependent EQE_{LED} measurements were performed on small-area CdTe cells and were found to be in agreement with theory. As expected, cells which exhibit major failure of light-dark J-V superposition did not follow trend of well-behaved cells.

EL images of selected defects from CdTe cells were discussed, and the images were shown to be highly sensitive to defects in devices, since the intensity depends exponentially on the cells' voltages. Six categories of cell defects were identified: weak-diode areas, cell delineated

in delete region, non-uniform Cl passivation, holes in back contact, high-resistance foreign layer, and a high back-contact sheet resistance. Each was discussed in detail with specific examples given. In most cases, additional opto-electronic characterization techniques were used to supplement the analysis of the EL images.

EL images of CSS-deposited CdS/CdTe modules manufactured by Abound Solar and similar to CSU CdTe cells were also investigated. Two types of defect were highlighted: a discontinuous P3 line scribe (intercell shunt) and a shunt through the CdTe cell (intracell shunt). The EL area affected by the intercell shunt was found to be much larger than that from the intracell shunt, partly due to the relatively low sheet-resistance of the metal back-contact. Both of these defect-types were shown to increase the affected EL area with decreasing voltage bias, though the effect of the intercell shunt dominated. This defect-type may be contrasted with a weak-diode area which was shown to not significantly effect area surrounding defect for voltage biases used. In addition, the EL intensity in the absence of defects was shown to be an accurate indication of the voltage drop across each cell in a module.

6.2 Recommendations for Future Work

Although in the work presented here, the EQE_{LED} -voltage deficit relationship was demonstrated to hold for many different cell types, future work should focus on additional demonstration of its universality and its limitations. To do so, absolute calibration of pixel response at the peak EL wavelength used needs to be performed, since the response of the detector array is reduced by ~ 0.13 abs.%/nm with increasing photon wavelength. The illumination source used (either a cell or a LED) should be of low optical power (as to not saturate the detector array), should not employ a focusing lens and should be calibrated with a photodiode.

Additional future work should also include a comprehensive investigation of how different defect-types in cells and modules can evolve with illumination and voltage bias at

elevated temperatures over an extended period of time. This use of EL may improve the understanding of some of the underlying degradation mechanisms in PV modules.

Defects which result in non-uniformities in a module's EL image such as a intracell shunt or a weak diode, can be analyzed using the technique developed by Koishiyev [30]. Furthermore, a defect's impact on module performance can be accounted for from its EL image, as discussed by others [30, 31]. These two techniques could be particularly helpful in the investigation of the evolution of defects in modules.

Bibliography

- [1] Jet Propulsion Laboratory. climate.nasa.gov, June 2015.
- [2] Rajendra K Pachauri, MR Allen, VR Barros, J Broome, W Cramer, R Christ, JA Church, L Clarke, Q Dahe, P Dasgupta, et al. *Climate Change 2014: Synthesis Report. Contribution of Working Groups I, II and III to the Fifth Assessment Report of the Intergovernmental Panel on Climate Change*. IPCC, 2014.
- [3] A.E. Rakhshani. Electrodeposited cdte-optical properties. *Journal of Applied Physics*, 81(12):7988–7993, 1997.
- [4] R.M. Geisthardt. *Device Characterization of Cadmium Telluride Photovoltaics*. PhD thesis, Colorado State University, 2014.
- [5] First Solar. <http://www.firstsolar.com/>.
- [6] A. Abbas, G.D. West, J.W. Bowers, P.M. Kaminski, B. Maniscalco, J. M. Walls, WS. Sampath, and K. L. Barth. Cadmium chloride assisted re-crystallization of cdte: The effect of the annealing temperature. In *Photovoltaic Specialists Conference (PVSC), 2013 IEEE 39th*, pages 356–361. IEEE, 2013.
- [7] Chen Li, Yelong Wu, Jonathan Poplawsky, Timothy J Pennycook, Naba Paudel, Wanjian Yin, Sarah J Haigh, Mark P Oxley, Andrew R Lupini, Mowafak Al-Jassim, et al. Grain-boundary-enhanced carrier collection in cdte solar cells. *Physical Review Letters*, 112(15):156103, 2014.
- [8] Brian E McCandless and Kevin D Dobson. Processing options for cdte thin film solar cells. *Solar Energy*, 77(6):839–856, 2004.
- [9] A Abbas, GD West, JW Bowers, P Isherwood, PM Kaminski, B Maniscalco, P Rowley, JM Walls, K Barricklow, WS Sampath, et al. The effect of cadmium chloride treatment

- on close spaced sublimated cadmium telluride thin film solar cells. In *Photovoltaic Specialists Conference (PVSC), Volume 2, 2012 IEEE 38th*, pages 1–6. IEEE, 2012.
- [10] ASTM Standard. G173, standard tables for reference solar spectral irradiances: Direct normal and hemispherical on 37 tilted surfaces. *Annual book of ASTM standards*, 12, 2009.
- [11] Simon M Sze and Kwok K Ng. *Physics of semiconductor devices*. John Wiley & Sons, 2006.
- [12] Martin A Green. Radiative efficiency of state-of-the-art photovoltaic cells. *Progress in Photovoltaics: Research and Applications*, 20(4):472–476, 2012.
- [13] T Kirchartz, U Rau, M Kurth, J Mattheis, and JH Werner. Comparative study of electroluminescence from cu (in, ga) se₂ and si solar cells. *Thin Solid Films*, 515(15):6238–6242, 2007.
- [14] John Raguse, J Tyler McGoffin, and James R Sites. Electroluminescence system for analysis of defects in cdte cells and modules. In *Photovoltaic Specialists Conference (PVSC), 2012 38th IEEE*, pages 448–451. IEEE, 2012.
- [15] Arthur Edelstein, Nenad Amodaj, Karl Hoover, Ron Vale, and Nico Stuurman. Computer control of microscopes using μ manager. *Current protocols in molecular biology*, pages 14–20, 2010.
- [16] Caroline A Schneider, Wayne S Rasband, Kevin W Eliceiri, Johannes Schindelin, Ignacio Arganda-Carreras, Erwin Frise, Verena Kaynig, Mark Longair, Tobias Pietzsch, Stephan Preibisch, et al. nih image to imagej: 25 years of image analysis. *Nature Methods*, 9(7), 2012.
- [17] <http://www.ccd.com/pdf/U8300.pdf>.

- [18] Matevž Bokalič, John Raguse, James R Sites, and Marko Topič. Analysis of electroluminescence images in small-area circular cdte solar cells. *Journal of Applied Physics*, 114(12):123102, 2013.
- [19] Matevž Bokalič and Marko Topič. *Spatially Resolved Characterization in Thin-Film Photovoltaics*. Springer, 2015.
- [20] Uwe Rau. Reciprocity relation between photovoltaic quantum efficiency and electroluminescent emission of solar cells. *Physical Review B*, 76(8):085303, 2007.
- [21] William Shockley and Hans J Queisser. Detailed balance limit of efficiency of p-n junction solar cells. *Journal of applied physics*, 32(3):510–519, 1961.
- [22] Jason M Kephart, Russell M Geisthardt, and WS Sampath. Optimization of cdte thin-film solar cell efficiency using a sputtered, oxygenated cds window layer. *Progress in Photovoltaics: Research and Applications*, 2015.
- [23] John M Raguse and James R Sites. Correlation of electroluminescence with open-circuit voltage from thin-film cdte solar cells. *IEEE Journal of Photovoltaics*, 2015.
- [24] Steve Johnston, Ingrid Repins, Nathan Call, Rajalakshmi Sundaramoorthy, Kim M Jones, and Bobby To. Applications of imaging techniques to si, cu(in,ga)se₂, and cdte and correlation to solar cell parameters. In *Photovoltaic Specialists Conference (PVSC), 2010 35th IEEE*, pages 1727–1732. IEEE, 2010.
- [25] Xufeng Wang and Mark S Lundstrom. On the use of rau’s reciprocity to deduce external radiative efficiency in solar cells. *IEEE Journal of Photovoltaics*, 3(4):1348 – 1353, October 2013.
- [26] John Raguse, Russell Geisthardt, Jennifer Drayton, and James R Sites. Compact accelerated life testing with expanded measurement suite. In *Photovoltaic Specialist Conference (PVSC), 2014 IEEE 40th*, pages 2644–2646. IEEE, 2014.

- [27] Kevin Eugene Walters. Computational fluid dynamics (cfd) modeling for cdte solar cell manufacturing. Master's thesis, Colorado State University, 2011.
- [28] Davis Robert Hemenway. Computational modeling of cadmium sulfide deposition in the cds/cdte solar cell manufacturing process. Master's thesis, Colorado State University, 2013.
- [29] Katherine Zaunbrecher. *Imaging as characterization techniques for thin-film cadmium telluride photovoltaics*. PhD thesis, Colorado State University, 2014.
- [30] G.T. Koishiyev. *Analysis of impact of non-uniformities on thin-film solar cells and modules with 2-D simulations*. PhD thesis, Colorado State University, 2010.
- [31] Anke Helbig, Thomas Kirchartz, Raymund Schaeffler, Jürgen H Werner, and Uwe Rau. Quantitative electroluminescence analysis of resistive losses in cu (in, ga) se 2 thin-film modules. *Solar Energy Materials and Solar Cells*, 94(6):979–984, 2010.